

Chapter 8

Natural Variability of Stratospheric Ozone

Lead Authors: Elisa Manzini & Katja Matthes

Co-Authors: Christian Blume

Greg Bodeker

Chiara Cagnazzo

Natalia Calvo

Andrew Charlton-Perrez

Anne Douglass

Pier Giuseppe Fogli

Lesley Gray

Junsu Kim

Kuni Kodera

Markus Kunze

Cristina Pena Ortiz

Bill Randel

Thomas Reichler

Gera Stenchikov

Claudia Timmreck

Matt Toohey

Shigeo Yoden

8.1 Introduction

Stratospheric ozone is known to vary in response to a number of natural factors, such as the seasonal and the 11-year cycles in solar irradiance, the Quasi-Biennial Oscillation (QBO), El Niño Southern Oscillation (ENSO), variations in transport associated with large-scale circulations (*i.e.*, Brewer-Dobson circulation) and dynamical variability associated with the annular modes. Aerosols from volcanic eruptions can also affect stratospheric ozone, although their effects depend on the background atmospheric composition. Ozone observations have demonstrated variations on a large number of spatial and temporal scales. To quantify the impact of anthropogenic perturbations to the ozone layer, and to make reliable projections of future ozone abundances, it is necessary to understand and to quantify the underlying natural ozone variations.

The goal of this chapter is to evaluate how well CCMs simulate natural stratospheric ozone variability, based on our current knowledge of the links between ozone variations and natural forcings. Fundamental questions are:

- Do the models realistically simulate natural ozone variations?
- Which processes are key in determining natural variability in stratospheric ozone?
- Do models that reproduce natural variations in ozone do so because these key processes are well simulated?

The response to these questions will inform the assessment of whether the models simulate natural ozone variations for the correct reasons.

The relative importance of the different sources of natural variability in stratospheric ozone is assessed here primarily by means of multiple linear regression analyses. When possible, the connection between the sources of natural variability and ozone is addressed by analysing the processes that determine it (see **Table 8.1**). Systematic inter-comparisons of ozone as simulated by the CCMs, as well as individual model studies, are considered. Evaluation of the CCMVal-2 REF-B1 simulations makes up the core of the assessment, while comparison of CCMVal-2 results with those from CCMVal-1 simulations is carried out when possible.

This chapter aims to synthesize the results of parts A and B of this report with respect to natural ozone variations. Trends related to anthropogenic ozone depletion are considered, in order to address the problem of how natural ozone variations are modelled but the discussion of the effects of these trends is left to Chapter 9.

8.2 Data and Methodology

8.2.1 Data

In the following, a brief description is provided of the key ozone and temperature observations employed to validate and assess the ability of the CCMs to simulate observed variability. To take into account the spread between available observational data sets and individual estimates of measurement errors, several data sets have been used, when possible.

The ground-based zonal mean column ozone data set from Fioletov *et al.* (2002; <ftp://ftp.tor.ec.gc.ca/Projects-Campaigns/ZonalMeans/>) and the merged satellite column ozone data set (TOMS/SBUV) from the Total Ozone Mapping Spectrometer (TOMS) and Solar Backscatter Ultraviolet 2 (SBUV/2) instruments (Stolarski and Frith, 2006; http://acdb-ext.gsfc.nasa.gov/Data_services/merged/) are used, because together they provide a long-term data set, ranging from 1964 to 2008. To construct the continuous data set, the ground-based data are used where no satellite data are available (1964-1979) and satellite data are employed where available (1980-2008). Gaps in the satellite data are filled with ground-based data (Fioletov *et al.*, 2002). This data set is referred to as “TOMS+gb”. The NIWA combined total column ozone database 1 for the shorter period 1980-2007 (updated from Bodeker *et al.*, 2005) is also employed, hereafter referred to as NIWA-column. The comparison of ground-based, merged satellite data, TOMS/SBUV data as well as the NIWA-column ozone data shows good correspondence between the 5 data sets and maximum differences of +1 to -1% (Fioletov *et al.*, 2002).

Several ozone profile data sets are employed. The Randel&Wu data set (Randel and Wu, 2007; 1979-2005) is based on output from a regression model applied to ozone anomalies from SAGE satellite data (referred to as Randel&Wu or SAGE in the following). The regression model includes a decadal trend (EESC: equivalent effective stratospheric chlorine), the QBO, 11-year solar cycle and an ENSO basis function, which are fitted to SAGE I and II satellite ozone anomalies. The regression output is added to a seasonal mean, zonal mean, vertically resolved ozone climatology (Fortuin and Kelder, 1998). The NIWA-3D data set (1980-2007) is based on satellite (SAGE I and II, POAM II, and III, HALOE) and ozone-sonde profiles where regression constrained interpolation has been used to produce a gap free data set (Hassler *et al.*, 2009). The NIWA-3D data set is similar to the Randel&Wu data set, in the sense that it is also the output of a regression model.

For the seasonal cycle studies of ozone, the Microwave Limb Sounder (MLS) data from the NASA Aura satellite (Waters *et al.*, 2006; Froidevaux *et al.*, 2008) are also em-

Table 8.1: List of diagnostics employed to evaluate the modelling of natural stratospheric ozone variability by the CCMs participating in CCMVal-2.

Process	Diagnostic	Variables	Data	References
Annual Cycle in Ozone				
Chemistry	Annual cycle at selected locations	O ₃ , T	MLS, HALOE	<i>Eyring et al. (2006)</i>
Chemistry & Dynamics	MLR analysis	O ₃	NIWA-3D	<i>Bodeker et al. (1998)</i>
	Annual cycle in column ozone	O ₃ column	NIWA-column	<i>Eyring et al. (2006)</i>
Interannual Polar Ozone Variability				
Dynamics & Transport	Monthly standard deviations and climatology	O ₃ column	NIWA-column	
	Heat flux relationship with column ozone	v'T', T	ERA-Interim, NIWA-column	<i>Weber et al. (2003)</i>
	Annular Mode relationship to column ozone	Z _g , O ₃	NCEP/NCAR, NIWA-column	<i>Hu and Tung (2002)</i>
Solar Cycle in Ozone				
Dynamics, Chemistry & Radiation	MLR analysis	T, O ₃	ERA-40, SSU, RICH, NIWA-3D, Randel&Wu	<i>Austin et al. (2008)</i>
Chemistry & Transport	MLR analysis	O ₃ column	NIWA-column, TOMS+gb	<i>Austin et al. (2008)</i>
Radiation & Chemistry	MLR analysis	SWHR - Short-wave heating rates	-	
QBO in Ozone				
Chemistry & Dynamics	Monthly standard deviations	U, O ₃	ERA-40, SAGE	<i>Baldwin et al. (2001)</i>
	MLR analysis	O ₃	NIWA-3D, Randel&Wu	
Transport, Dynamics & Chemistry	MLR analysis	O ₃ column	NIWA-column, SAGE, TOMS+gb	
ENSO Signal in Ozone				
Dynamics & Transport	MLR analysis	T, O ₃	ERA-40, RICH, NIWA-3D, Randel&Wu ozone	<i>Free and Seidel (2009); Randel et al. (2009b)</i>
	Composite analysis	T, O ₃ column	ERA-40, NIWA-column	<i>Cagnazzo et al. (2009)</i>
Volcanic Aerosols				
Radiation & Chemistry	Composite analysis	T, O ₃ column	ERA-40, NIWA-column, TOMS+gb	<i>Timmreck et al. (2003)</i>
	MLR analysis	T	ERA-40, SSU, RICH, NIWA-3D, Randel&Wu	
Chemistry & Transport	Composite analysis	ClO, O ₃		

ployed. The MLS instrument has made global measurements nearly every day since August 2004 and is therefore ideal for examining the seasonal cycle at various pressure levels. Monthly averaged values of MLS ozone are computed for 6-degree latitude bins. The ozone climatology for the period 1991-2002 from the Halogen Occultation Experiment (HALOE) onboard the Upper Atmosphere Research Satellite (UARS; Russell *et al.*, 1993) is also used. Data after September 2002 have not been included because of the unusual major warming in the Antarctic in 2002, and because the observations have been less frequent since 2002 (Grooß and Russell, 2005).

Various temperature data sets are used: 1) SSU (Stratospheric Sounding Unit) temperature data for the middle and upper stratosphere (Randel *et al.*, 2009a; 1979-2005), 2) the Radiosonde Innovation Composite Homogenization (RICH) data set that uses the ERA-40 reanalysis to identify break points, which are then adjusted using neighboring radiosonde observations in the lower stratosphere and troposphere (Haimberger *et al.*, 2008; http://www.sparc.sunysb.edu/html/updated_temp.html; 1960-2004), and 3) the ERA-40 reanalysis temperature data (Uppala *et al.*, 2004; 1979-2001). The reanalyses are used to allow comparison of similar spatial coverage as in the CCMs, keeping in mind the uncertainties related to possible spurious trends in this data set (for a discussion see *e.g.*, Randel *et al.*, 2009a).

8.2.2 Multiple Linear Regression Analysis

Multiple linear regression (MLR) analyses is a commonly used method to assess the relative contributions of different drivers of variability in geophysical time series, *e.g.*, near global total column ozone (Chapter 3 in WMO, 2007). Here we compare results from an MLR analysis applied to monthly ozone and temperature fields from the REF-B1 simulations of CCMVal-2 with results from an identical analysis of the appropriate observational data sets described above. Although the focus is on sources of natural variability (annual cycle, solar cycle, QBO, ENSO, and volcanoes), a secular term is also required to account for the substantial trend in ozone and temperature over the period examined. For the ozone regression, the secular term is represented by the EESC (equivalent effective stratospheric chlorine), while for the temperature regression, a linear trend is used instead. The MLR analysis is based on the method described in Bodeker *et al.* (1998, 2001) to model a time dependent variable, *e.g.*, ozone:

$$y(t) = \beta_{\text{offs}(N=4)} \times \text{offset} + \beta_{\text{EESC}(N=2)} \times \text{EESC}(t) + \beta_{\text{QBO}(N=2)} \times \text{QBO}(t) + \beta_{\text{QBO_orthog}(N=2)} \times \text{QBO_orthog}(t) + \beta_{\text{sol}(N=0)} \times \text{solar}(t) + \beta_{\text{ENSO}(N=2)} \times \text{ENSO}(t) + \beta_{\text{Ag}(N=2)} \times \text{Agung}(t) + \beta_{\text{Elc}(N=2)} \times \text{ElChichon}(t) + \beta_{\text{Pin}(N=2)} \times \text{Pinatubo}(t) + R(t)_{t=1,n}$$

The first term in the regression model (β_{offs} coefficient times the offset basis function) represents a constant offset and, when expanded in a Fourier expansion, represents the mean annual cycle. In this case, with four Fourier pairs ($N=4$ in the equation above), the annual cycle is modelled as a summation of 12, 6, 4, and 3 month harmonics each of variable phase. All basis functions are de-trended except for the EESC, the trend and volcano basis functions; and the offset is removed from the respective basis functions except for the volcanoes. The sensitivity of the basis functions to different numbers of Fourier pairs was tested. The two Fourier pair expansion for the EESC fit coefficients was chosen to account for the strong seasonal cycle in the effect of EESC on ozone, particularly in the polar regions. For all other basis functions the results are not significantly influenced by changing the number of Fourier expansions of their fit coefficients.

The EESC basis function represents the total halogen loading of the stratosphere effective in ozone depletion, appropriately weighted by the mean age of air (age 3.0 years and width 1.5 years has been selected for the global average investigated here). For most of the CCMs, the EESC has been calculated using the formula suggested by Newman *et al.* (2007): $\text{Cl}_y + 60\text{Br}_y$ (in volume mixing ratio (vmr)) and the global monthly mean values at 50 hPa, and is referred to as effective stratospheric chlorine (ESC) in Eyring *et al.* (2007). Some CCMs do not provide Cl_y and/or Br_y and therefore for these CCMs the observed EESC is used (E39CA, NiwaSOCOL, UMUKCA-METO, and UMUKCA-UCAM). The EESC fit coefficient (β_{EESC}) represents the anthropogenic part of the signal and is not discussed until the Chapter 9. Note that an additional linear trend term for the ozone regression is not included, because it is assumed that all long-term secular changes within the last 50 years are captured by the EESC basis function.

The QBO basis function is specified as the monthly mean 50 hPa zonal wind (except for AMTRAC3 where 10 hPa and UMSLIMCAT where 30 hPa is used) for each individual model realisation. Since the phase of the QBO varies with latitude and altitude a second QBO basis function is included, which is orthogonal to the first, as described by Austin *et al.* (2008). For the CCMs in Group A of Table 8.4, the QBO basis function is neglected, given their lack of interannual variability in the tropics (see Figure 8.14).

The observed Nino 3.4 sea surface temperature (SST) anomalies are used for the ENSO basis function without a time shift. The F10.7cm radio flux is employed for the 11-year solar cycle basis function. The volcanic aerosol basis functions for Agung, El Chichón and Pinatubo are taken from Bodeker *et al.* (2001). To account for the autocorrelation in the residuals, an autoregressive model of R (the residual) is used: First a fit to the time series is performed and a residual calculated. Then the autocorrelation coefficient is calculated using Equation 6 in Bodeker *et al.* (1998) and

used to transform the basis functions and the regression time series. The MLR analysis is then applied a second time and now includes the effects of autocorrelation in the residuals. Uncertainties are expressed as the square root of the sum of the squared diagonal elements of the covariance matrix.

In summary, only the QBO and the EESC basis functions are formed from model output. All the other basis functions are common to the MLR analyses of both the time series from the CCMs and observational data.

In **Figure 8.1** the contribution of the various natural as well as anthropogenic contributions to global (60°S-60°N) column ozone variations is shown for the ground-based data set in Dobson units. Figure 8.1 shows that the observed long-term decrease in column ozone is almost completely explained by the trend due to increased atmospheric halogen loading. However, natural variability is not negligible. The annual cycle dominates the natural variability with an amplitude of ~12 DU, followed by the 11-year solar cycle with ~6 DU between solar maximum and solar minimum, the QBO with ~4 DU between maximum QBO easterlies and westerlies, a small component associated with ENSO of ~1 DU, and the volcanic contribution which has distinct and unevenly distributed contributions of up to 6 DU. Note that the residual, especially before the satellite era is relatively large (up to ± 5 DU) and we can only speculate that this has to do with the data quality. Also we emphasize that the atmosphere is highly non-linear, so the residual represents to some extent also the failure of a linear regression analysis to account for non-linear processes in the atmosphere.

The results of the MLR analysis are presented in the following Sections (8.3-8.8), together with process oriented studies. For most CCMVal-2 models the whole time series from 1960 to 2004 is considered (although some only provide data up to 2000). Comparisons with observations are also described, employing data for the same time period (1960-2004) or only from the satellite era (1979-2007), as appropriate. In these cases, the sensitivity of the MLR analysis to the selected time period has been tested (but is not shown); unless otherwise stated, the essential results are not substantially affected by the shortened period, although the amplitude of the signal is usually larger.

8.3 Annual Cycle in Ozone

Pronounced variations in stratospheric ozone are caused by annual variations in transport and photochemistry. The transport variations are driven by dynamical processes (Chapters 4 and 5) and can affect ozone either directly or indirectly (through changed transport of ozone-depleting substances). Photochemical production of ozone depends on annual variations in the solar irradiance (Chapters 3 and

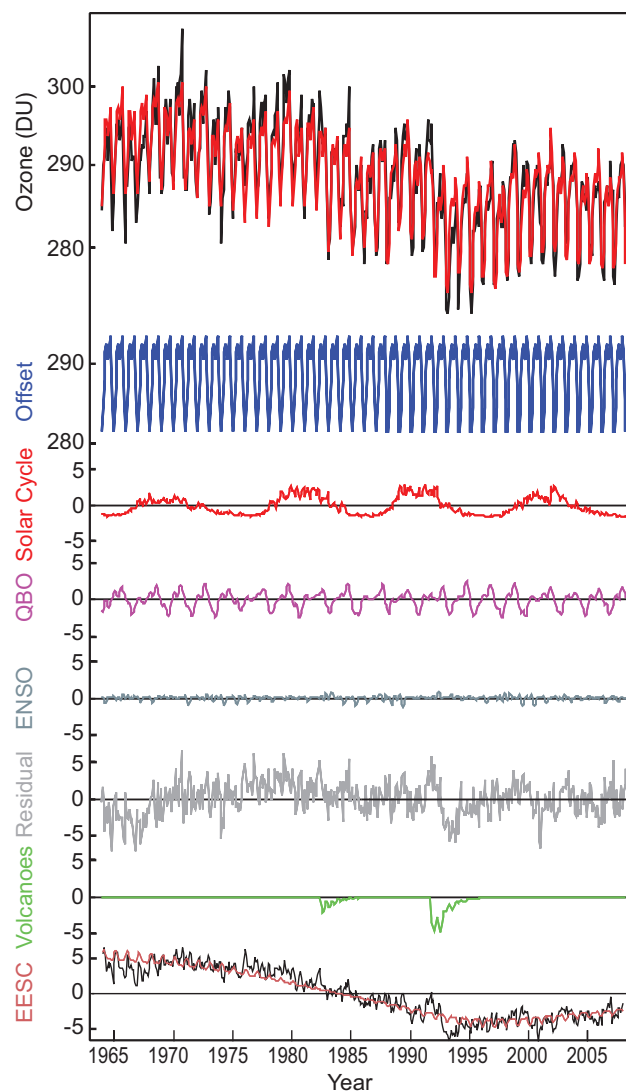


Figure 8.1: Ozone variations for 60°S-60°N in DU estimated from ground-based measurements (Fioletov et al., 2002) and individual components that comprise ozone variations, from 1964 to 2008. From top to bottom: Original data (black) and fitted with a multiple linear regression (MLR) model (red); annual cycle (blue); 11-year solar cycle (red); QBO (purple); ENSO (light blue); residual (grey); and the EESC (red) curve scaled to fit the data from 1964-2008. The residual is the difference between the original and the fitted time series. See text for details on the MLR analysis.

6). The resulting annual cycle in column ozone is characterized by (a) low amounts in the tropics year-round, (b) maxima in the spring of Northern Hemisphere (NH) high latitudes and Southern Hemisphere (SH) middle latitudes, and (c) larger hemispheric-mean amounts in the NH *versus* the SH. This annual evolution of column ozone reflects the dominant influence of transport processes on lower stratospheric ozone.

8.3.1 Annual cycle at selected locations in the stratosphere

The photochemical time scale for ozone varies seasonally as a function of latitude and pressure. In the lower stratosphere the time scale is long and the seasonal cycle is largely controlled by transport. In the upper stratosphere, the time scale is short and the ozone mixing ratio reflects a near balance between production and loss. Since the time scales for transport and for photochemical processes both vary seasonally, in some parts of the stratosphere both types of process contribute to the stratospheric concentration of ozone. For example, in winter transport processes control the seasonal build-up of ozone through descent at the edge of the vortex and this is then moderated at high latitudes during cold winters by chemical loss associated with polar processes. In summer, transport effects are minimal and the photochemical time scale decreases from several years to 30 days or less, producing a summer minimum that varies little from year to year.

In **Figure 8.2** the annual cycle in ozone mixing ratios simulated by 16 CCMs is compared with MLS observations. At 1 hPa the time evolution of monthly-mean, zonal-mean ozone is shown at 40°S, the Equator and 40°N. At 46 hPa corresponding plots are shown for 72°S, the Equator, and 72°N. Four separate years of MLS observations are shown in the SH and equatorial plots (January 2005-December 2008) and three years (July 2005-June 2008) are shown in the NH; the NH observations are phase shifted to align the seasons with those of the SH observations. From the models, only a single year's annual cycle is shown, taken from the early 2000s for consistency with the data. Examination of up to an additional 10 years per model (not shown) has demonstrated that the comparisons are representative. The annual mean has been subtracted in all figures to emphasize the seasonal variation in both observations and simulations.

Although the ozone column is dominated by mixing ratios in the lower stratosphere and hence its annual cycle is barely affected by the evolution of upper stratosphere

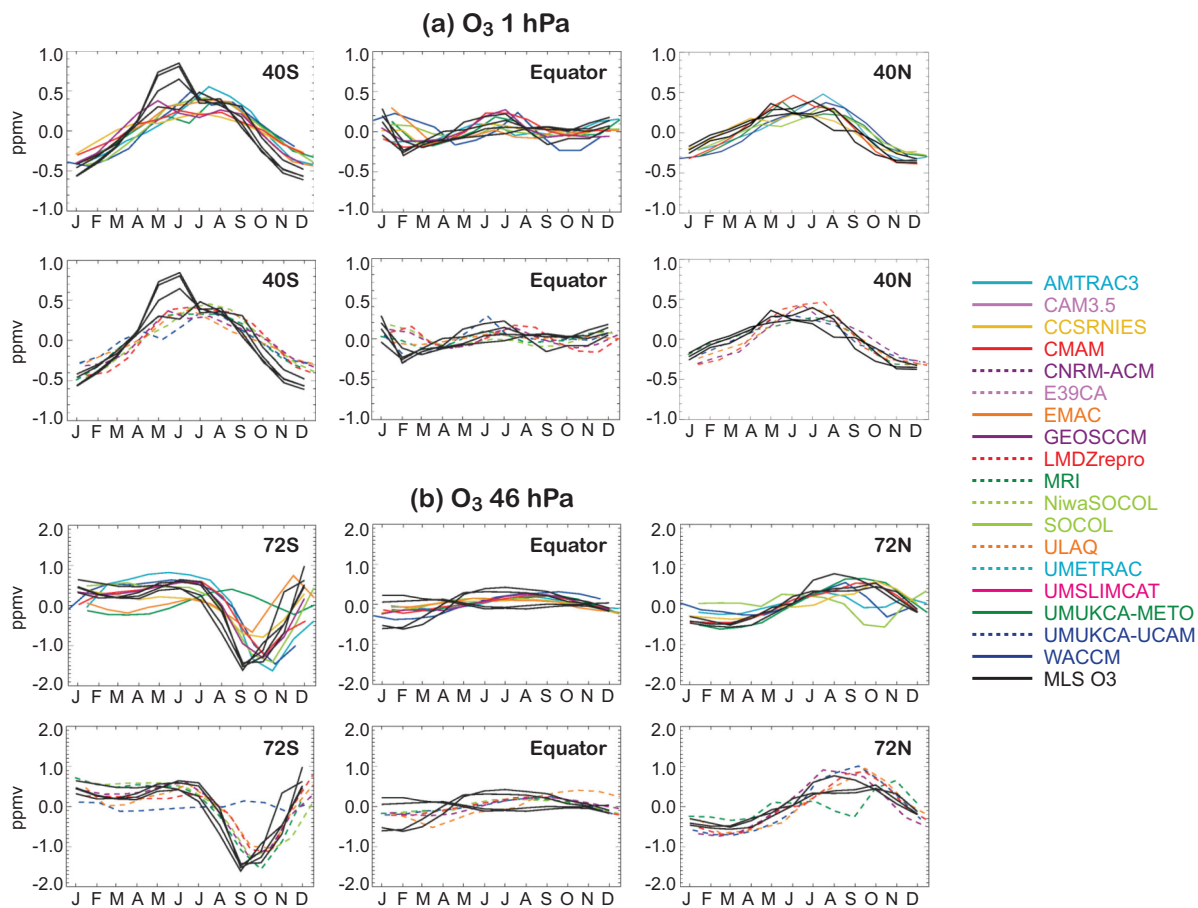


Figure 8.2: (a) Monthly mean ozone mixing ratios (ppmv) at 1 hPa throughout the year, 40°S (left), equator (middle) and 40°N (right) from several years of MLS observations (black lines) and for the CCMVal-2 CCMs (monthly zonal-mean ozone in the early 2000s from selected years). MLS data are averaged for a six degree latitude band centred on the selected latitudes. (b) Same as 8.2a but at 46 hPa, 72°S (left), Equator (middle) and 72°N (right).

mixing ratios, a comparison at 1 hPa provides a simple check on the performance of the photochemical schemes implemented in the various models (see also the more detailed comparison of photochemical schemes in Chapter 6). The simulated annual cycle at both 40°S and 40°N generally approximates the MLS data. The simulated annual cycle in temperature also agrees with observations (Figure S8.1 in the supplementary material), so this comparison verifies the simulated sensitivity to temperature. A positive anomaly in the SH during May and June in the MLS data is not reproduced by any model. A similar (negative) feature in temperature mirrors this anomaly. In the tropics, a small semi-annual oscillation is also seen in the observations. Many of the models also reproduce this semi-annual variation but with differences in the timing. This phase difference between models and observations is also seen in the temperature variations (Figure S8.1) and therefore explains the mismatch in ozone. To summarize, the models exhibit the appropriate sensitivity to temperature, so, when the simulation reproduces (or does not reproduce) the tem-

perature variation, a corresponding match or mismatch is seen in the ozone variations.

At 46 hPa during winter and spring in the high latitude SH, the ozone mixing ratio anomaly is dominated by polar ozone loss. Figure 8.2 (bottom) shows that the models generally reproduce this variation, except for UMUKCA-METO and UMUKCA-UCAM. For both of these models, there is polar ozone loss, but it does not extend as far equator-ward as 72°S. Note that these models perform better further south. While observations show a peak ozone loss in September, the CCMs response is shifted by one to two months. At the equator, the MLS data show a seasonal variation that depends on the phase of the QBO and is not fully captured by the models (see Section 8.6). In the NH, transport and polar ozone destruction processes control the evolution during winter/spring. Both contribute to the substantial observed variability in ozone during these seasons. Interannual variability in winter/spring is so large (see Section 8.4) that differences between the observations and simulations are not significant. However, during the

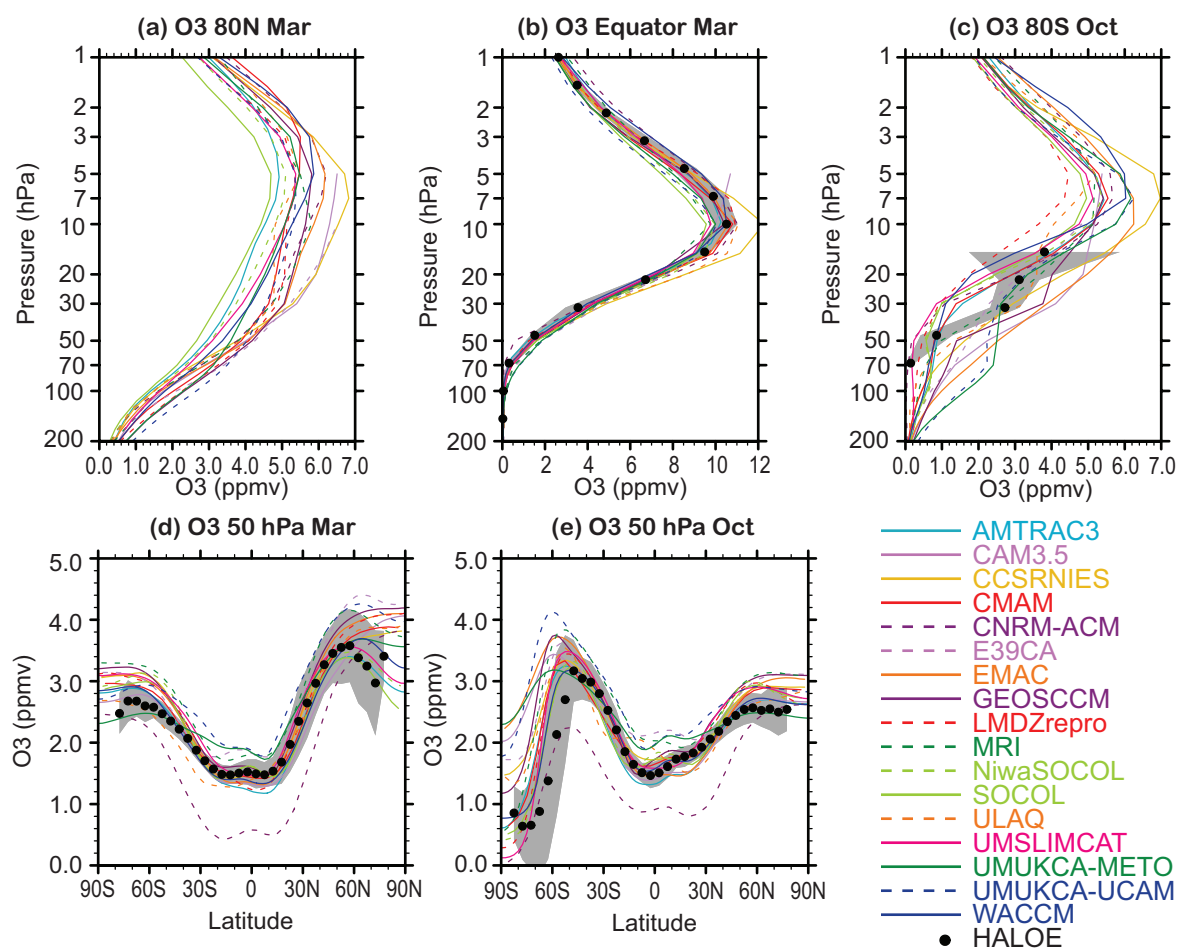


Figure 8.3: Climatological zonal mean O_3 mixing ratios from the CCMVal-2 CCMs and HALOE in ppmv. Vertical profiles at (a) 80°N in March, (b) 0° in March, and (c) 80°S in October. Latitudinal profiles at 50 hPa in (d) March and (e) October. The grey area shows HALOE ± 1 standard deviation (s) about the climatological zonal mean. Same as Figure 13 for CCMVal-1 CCMs in Eyring et al. (2006).

summer the photochemical time scale decreases to 30–60 days, the circulation is near zonal with little horizontal or vertical mixing and the ozone mixing ratio is close to photochemical balance. The interannual variability of the observed ozone mixing ratio during this period is minimal. In the models, there is a relatively large spread during this period (and also during January–February–March in the SH), which likely reflects the spread of temperatures between the models (see Chapter 4). Nevertheless, the simulated ozone mixing ratios return to values that are the same each year within a few percent in each of the last 10 years of the integrations (not shown), in agreement with the observations, thus demonstrating that models make a reasonable transition to photochemical control in summer. This variation decreases with increasing pressure; at 70 hPa the models reproduce the observed small annual variation in ozone mixing ratio (not shown).

8.3.2 Springtime ozone values

Figure 8.3 compares climatological mean vertical ozone profiles and latitudinal cross-sections in March and October derived from the CCMVal-2 models and HALOE observations (see Figure 13 from Eyring *et al.*, 2006 for the CCMVal-1 models). At the equator, most models agree well with HALOE observations and lie within one standard deviation of the HALOE mean, except for the CCSRNIES model that shows unusually large ozone peak values at 10 hPa. At higher latitudes during NH and SH spring there is a larger spread between the models and only a few lie within one standard deviation of the HALOE mean. This is especially true in the lower stratosphere/upper troposphere where CCMVal-1 simulations showed very good agreement with observations but CCMVal-2 simulations show a much larger spread. This may be simply because more CCMs now participate in CCMVal-2; see also Chapter 7 for a detailed discussion on UTLS performance of each model.

In the SH spring, the vertical profiles of CCSRNIES, CAM3.5, EMAC, UMUKCA-METO, and UMUKCA-UCAM are biased high, while LMDZrepro is biased low. In the NH, again CCSRNIES and CAM3.5 are biased high, while SOCOL is biased low. For the CCSRNIES model, the overestimation of peak ozone values in the tropics and polar regions was already evident in CCMVal-1 and is related to overestimation of O_2 photolysis rates at this altitude (see PhotoComp results in Chapter 6, *e.g.*, Figure 6.1). The pronounced ozone bias that was evident in LMDZrepro in CCMVal-1 has been improved but this model is still biased low due to the warm temperature bias in the SH (Chapter 4).

The lower panels of Figure 8.3 show that the latitudinal representation of ozone in the lower stratosphere in spring-time of each hemisphere has improved since

CCMVal-1. Between 60°S and 60°N most models lie within one standard deviation of the HALOE data. The CNRM-ACM is a clear outlier and substantially under-estimates the values. At polar latitudes more than half of the CCMs significantly overestimate the HALOE ozone values, possibly related to their low potential for chlorine activation (PACI; Chapter 6, Table 6.5). SOCOL, NiwaSOCOL, AMTRAC3, UMSLIMCAT, and WACCM agree best with observations at northern high latitudes in March, while at southern high latitudes CNRM-ACM and LMDZrepro are equally good compared to observations.

8.3.3 Annual cycle metrics

Differences between modelled and observed annual cycles in ozone can be further quantified by means of normalised Taylor diagrams (Taylor, 2001). The usefulness of the Taylor diagrams is their compact representation of pattern statistics between two fields, thus providing a straightforward methodology to quantify and compare results from a large number of fields (model diagnostics) with respect to a reference field (observations). The pattern statistics computed are correlations and normalised spatial standard deviations, respectively giving information on the differences in phase and magnitude, between each model result and the observation. In the Taylor diagram, the correlation is given by the cosine of the angle from the x-axis, and the normalised spatial standard deviation is the radial distance from the origin. The observation (reference) point therefore lies on the x-axis, with standard deviation equal to 1 and correlation equal to 1. The distance from the reference point (curved dashed lines with the origin at the reference point) measures the centred root mean square error.

The normalised Taylor diagram for the annual and the semi-annual harmonics of the zonal-mean ozone from the MLR analysis is shown in **Figure 8.4**. Since the focus is on stratospheric ozone, the pattern statistics are computed for the latitude-pressure sections ranging respectively from the South to the North poles, and from 500 to 1 hPa pressures; and the pattern statistics calculation includes area weights, but no weighting in pressure. Therefore, Figure 8.4 evaluates the latitude-pressure patterns of the modelled annual and semi-annual harmonics, namely the fields shown in the supplementary material (Figures S8.2–S8.4). Figure 8.4 shows that both the annual and the semi-annual harmonics in zonal mean ozone are very well represented for the majority of models, with respect to the NIWA-3D ozone data set. All models are characterized by correlations higher than 0.8, except for one model, E39CA in the case of the annual harmonic and CAM3.5 in the case of the semi-annual harmonic. Interestingly, both E39CA and CAM3.5 are the models with low tops (Chapter 2), suggesting that the top boundary conditions applied in these models may slightly degenerate the performance of their annual cy-

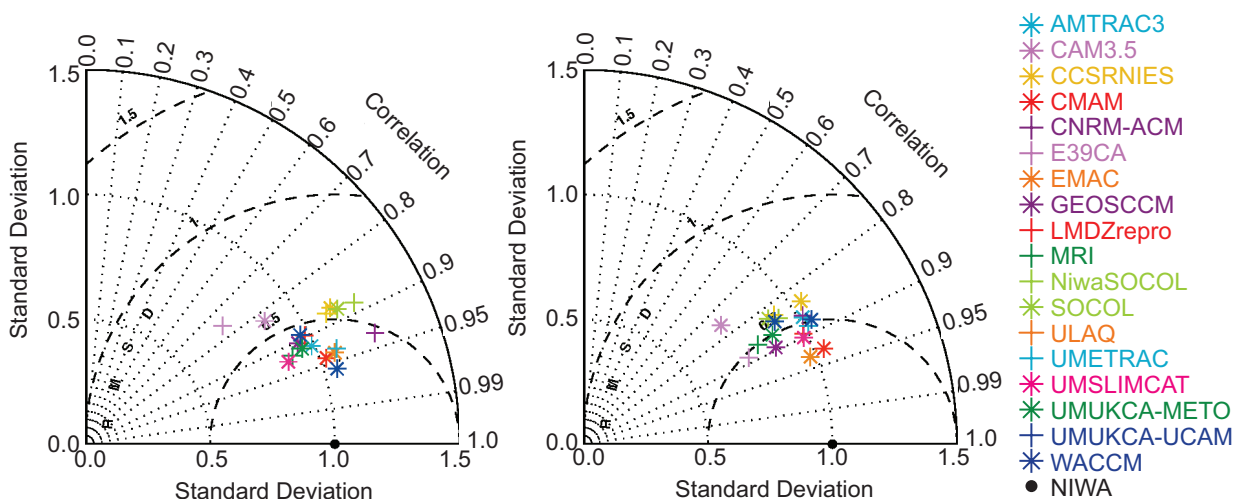


Figure 8.4: Normalised Taylor diagram of the annual (left) and semi-annual (right) harmonics of the zonal-mean ozone, latitude-pressure distribution, for the NIWA-3D data set and the CCMVal-2 models. The corresponding fields are shown in the supplementary material (Figures S8.2–S8.4). The pattern statistics have been computed for the 1–500 hPa, 90°S–90°N range.

cle in ozone. The relative clustering of the model points around one standard deviation demonstrates also that the magnitudes of the modelled spatial ozone variations compare well to those of the NIWA-3D data set.

For comparison with the performances of the annual and semi-annual cycle, the normalised Taylor diagram of the annual zonal-mean ozone coefficients from the MLR analysis is reported in the supplementary material (Figure S8.5). In this case, the very close clustering of the model signatures around the black solid point on the x-axis, which is the reference observation, demonstrate that the annual zonal-mean ozone field is extremely well simulated by all models.

The evaluation of the annual cycle in column ozone is performed on the monthly-mean zonal-mean model data. For the models, only data from 1980 to the end of the REF-B1 simulations (which vary model by model between 2000 and 2007) are considered, to better match the period of the NIWA-column ozone data set (1980–2007) used as the reference field. A second data set, the TOMS+gb column ozone since 1980 has also been used to provide an estimate of the uncertainty in the observations. In addition, plotting each available realization from the models shows the sample uncertainty. The normalised Taylor diagram from these data, using NIWA-column ozone as the reference, is shown in Figure 8.5. Therefore, Figure 8.5 evaluates the latitude-month patterns of the modelled column ozone fields, shown in supplementary material (Figure S8.6). Note that the Taylor diagram is computed only for data between 60°S and 60°N (for the annual cycle in polar ozone, see Section 8.4). Figure 8.5 demonstrates that most models capture the phase of the annual cycle and the latitudinal distribution of the total ozone quite well. All

models are characterized by correlations close to or above 0.9. Only UMUKCA-UCAM overestimates the spatial standard deviation substantially (factor 1.5), while CNRM-ACM under-estimates it. As a group, the models display a slight overestimation of the seasonal variations of the zonal mean column ozone (most model points have standard deviations between 1 and 1.5)

In the computation of the Taylor diagram, the mean bias is excluded. The relative mean bias, (model – observation)/observation, is shown for the near global column ozone and the northern and southern polar caps in Table

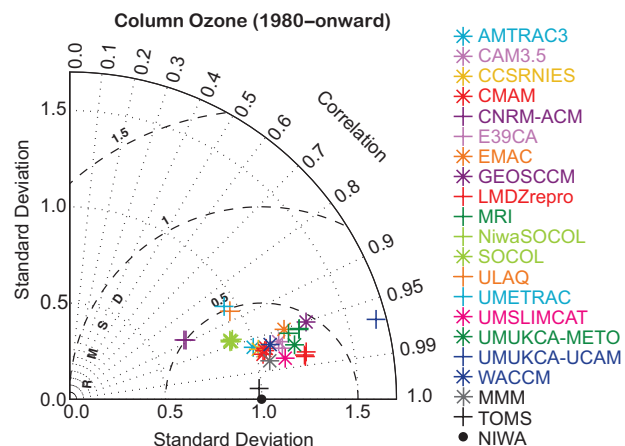


Figure 8.5: Normalised Taylor diagram of the annual cycle of the zonal-mean column ozone, latitude-month distribution, for the NIWA-column and TOMS+gb data sets and the CCMVal-2 models. The corresponding fields are shown in the supplementary material (Figure S8.6). The pattern statistics have been computed for the 60°S–60°N range.

8.2. The NIWA-column ozone is used as the reference observations. For most models, the relative mean bias is small, within a few percent. Defining as outliers the models with an absolute relative mean bias larger than 10%, it is found that E39CA and UMUKCA-UCAM overestimate the near-global ozone and both the North and South polar ozone; UMSLIMCAT slightly under-estimates only the near global ozone; GEOSCCM and UMUKCA-METO overestimate ozone over both polar caps; LMDZ-repro and UMETRAC respectively over- and under-estimate ozone only in the northern polar cap; CAM3.5, EMAC, and MRI overestimate ozone and CNRM-ACM under-estimates ozone over the southern polar cap.

8.4 Interannual Polar Ozone Variability

In the extra-tropics, interannual natural variations in stratospheric ozone are largest in the polar regions and tend to maximise during the spring season. **Figure 8.6a** (top panels) shows the monthly interannual standard deviation of column ozone averaged over the polar caps (60°N-90°N at left and 60°S-90°S at right), from the CCMVal-2 models and the NIWA-column ozone data. The corresponding annual cycle in the column ozone climatology is shown in Figure 8.6b. These results have been calculated for the time period from 1980 to the end of the REF-B1 simulations (varying model by model, between 2000 and 2007) and for 1980-2007 for the NIWA-column data. For the models, similar results were obtained if the calculation is performed from 1960 (not shown). Prior to the calculation of the diagram shown in Figure 8.6a, decadal trends were removed from the data. This was accomplished by calculating a low-pass filtered version of the data (the time filter consists of Gaussian-weighted running means with a full width at half maximum of 9 years) and by removing it from the original time series. The resulting time series therefore, contain only variability on time scales from 1 to about 10 years. Model performance with respect to the NIWA-column data is quantified by corresponding Taylor diagrams (Figure 8.6 lower panels).

Figure 8.6a shows that the interannual variability of the NIWA-column ozone exhibits a pronounced annual cycle and maximises during the dynamically active late winter and early spring periods of each hemisphere (January-April in the NH; August-November in the SH). The simulation of this observed seasonality represents an important model benchmark. Figure 8.6a demonstrates that all models show a minimum in variability in the late summer and fall (upper panels) and that the correlation coefficient is above 0.7-0.8 for most of the models (lower panels). Better agreement with the NIWA-column data may not be warranted, because at polar latitude during winter the NIWA-column data are mostly estimates (Bodeker *et*

Table 8.2: Total ozone model bias in % for different latitude ranges.

CCM	60°S-60°N	60°N-90°N	90°S-60°S
AMTRAC3	-3.77	-6.57	-0.36
CAM3.5	-3.64	1.79	11.07
CCSRNIES	5.86	1.51	9.12
CMAM	-2.18	0.04	-1.18
CNRM-ACM	-5.81	-3.12	-14.95
E39CA	15.14	19.07	16.04
EMAC	2.02	2.71	13.94
GEOSCCM	3.33	15.72	19.37
LMDZrepro	4.31	10.67	2.30
MRI	8.88	9.92	15.11
NiwaSOCOL	0.77	-3.34	-4.42
SOCOL	-1.49	-5.85	-6.49
ULAQ	3.29	-1.65	-4.45
UMETRAC	-3.95	-13.95	-0.03
UMSLIMCAT	10.34	-4.80	-5.87
UMUKCA-METO	6.61	12.84	16.65
UMUKCA-UCAM	14.07	26.26	34.40
WACCM	-2.35	2.26	-5.68
MMM	1.71	3.53	5.25

al., 2001, 2005).

During the NH active period (Figure 8.6a left panel), the amplitude of the annual cycle is well simulated by most models, with notable exceptions for MRI, which exhibits very large variability and standard deviation larger than 2 in the Taylor diagram, and also UMUKCA-UCAM and WACCM, both with standard deviation close to 1.5 in the Taylor diagram. The rest of the models are close together and slightly under-estimate the observed total ozone variability, suggesting a possible systematic bias. The results for individual ensemble members of MRI (not shown) are very similar, indicating that its high variability is not due to sampling uncertainty. The interannual variability of the WACCM model, in addition to be biased high, is characterized by a prolonged period of high variability, extending into June (low correlation, below 0.6).

During the SH active period (Figure 8.6a right panel), the model results tend to surround the observations. Models with particularly low variability are CNRM-ACM, E39CAA, GEOSCCM, and UMUKCA-UCAM. Models with particularly high variability, suggesting an early start of the active period, are CAM3.5 and EMAC, while CMAM has excessive variability in November.

The annual cycle of the column ozone climatology averaged over the polar caps (Figure 8.6b) shows the NH

spring time column ozone build up and the seasonality of the SH ozone hole. The timing of the NH ozone build up is well simulated by all models, as quantified by correlations above 0.8 for all models (bottom panel). A weak build up is noted for NiwaSOCOL, SOCOL, and possibly AMTRAC3 and MRI. In the SH, the situation is complicated by the presence of the ozone hole, an anthropogenic modification of the annual cycle. Therefore, factors such as the size of the polar vortex (a dynamical process), the strength of the polar barrier, as well as heterogeneous chemistry (a chemical process) play a role in determining the large spread of modelled column ozone minimum in September–October, as discussed in Chapter 6. Particularly low correlations (below 0.5) are displayed by E39CA, EMAC, UMUKCA-METO, UMUKCA-UCAM, and WACCM. Of these models, only WACCM reproduces the dip in ozone, *albeit* with a 2-month delay. The other highlighted outliers instead fail to model the impact of the ozone hole on the annual cycle. Among the models that better reproduce the column ozone annual cycle, NiwaSOCOL, MRI, and SOCOL overestimate its amplitude (standard deviations larger than 1.5, bottom panels). Note that the CAM3.5 model is not plotted, because it falls outside the Taylor diagram (standard

deviation: 0.8; correlation coefficient: -0.4).

In addition, Figure 8.6b (upper panels) shows that a number of models are affected by a mean bias in polar column ozone, which cannot be quantified by the Taylor diagram. In the NH, E39CA and UMUKCA-UCAM column ozone fields are biased high, while UMETRAC column ozone is biased low (see Table 8.2), in spite of their high correlations and standard deviations close to 1 (implying well simulated phase and magnitude of the annual cycle). These biases may be related to excessive stratosphere to troposphere ozone transport and/or tropospheric chemistry. In the SH, the E39CA, EMAC, GEOSCCM, MRI, UMUKCA-METO, and UMUKCA-UCAM ozone fields are all biased high (see Table 8.2).

The winter and spring evolution of the interannual variability in column ozone is associated with the seasonality of planetary wave activity and its influence on the strength of polar descent in the Brewer-Dobson circulation (Fusco and Salby, 1999, Randel *et al.*, 2002). When planetary wave activity is high, diabatic descent at high latitudes is strengthened, leading to increased transport of ozone-rich air from the tropical middle stratosphere (where ozone is photochemically produced) to the polar

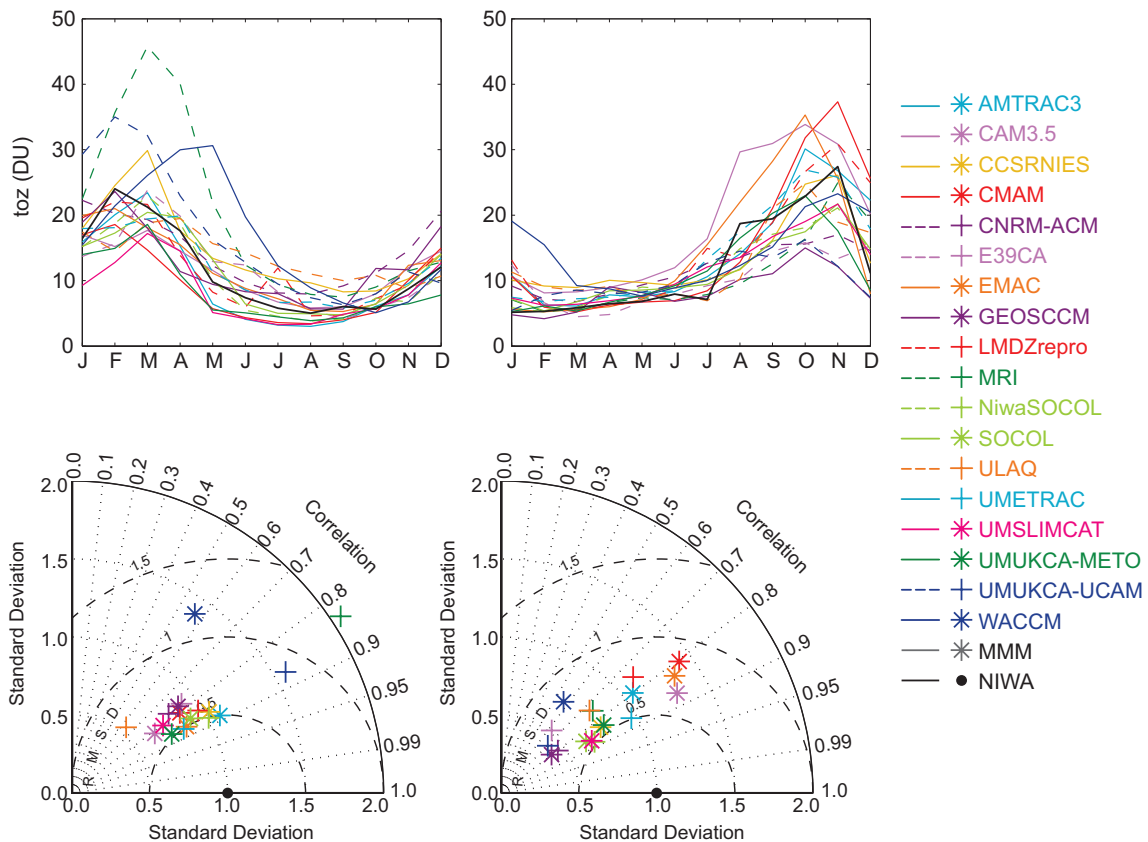


Figure 8.6a: Interannual variability of polar cap averaged column ozone (DU, upper panels) and corresponding normalised Taylor diagrams (lower panels) for NH (left) and SH (right) over the period onward of 1980. Legend for model results in the upper panels: Star (cross) symbols correspond to solid (dashed) lines. Black solid line represents NIWA-column data.

lower stratosphere. In addition, increased wave activity leads to a more disturbed polar vortex and hence to higher polar temperatures, creating less favourable conditions for chemical depletion of ozone due to heterogeneous processes. To evaluate the modelled connections between ozone variability and dynamical variability (the latter discussed in Chapter 4), the relationships between column ozone and, respectively, meridional heat fluxes, temperature and the stratospheric annular mode are reported in the following sections.

8.4.1 Heat flux and column ozone

Weber *et al.* (2003) show a compact relationship between the spring-to-fall ozone ratio in each hemisphere and the winter-time mean heat flux. In this section the presence of a similar relationship is investigated. The models are compared to observations using winter-time mean 100 hPa meridional heat fluxes from the ERA-Interim data set and the spring-to-fall ratio in column ozone from the NIWA-column ozone data. Column ozone ratios are for March/September in the NH and September/March in the SH, using area weighted averages between 60° and the pole.

Heat fluxes are averaged between 45° and 75°, using extended winter means: September-March (NH) and March-September (SH). SH data are de-trended as previously for Figure 8.6a. To calculate the spring-to-fall ozone ratio it is necessary to add a climatological ozone field to the filtered time series: a 10 year mean, monthly column ozone amount (1990-2000) was employed for this, since it is a period common to both the data and models. The analysis is performed for every year of model data from 1960 to the end of each simulation (which varies from model to model, between 2000 and 2007) and for 1980-2007 for NIWA-column and ERA-Interim data.

Results from the individual scatter plots (see supplementary material Figures S8.7) are summarized in **Figure 8.7**, where the slope parameter of the linear fit of each scatter plot is plotted against the mean spring-to-fall ozone ratio for each model or data set, along with the 95% confidence interval of the slope parameter. The slope of the scatter plot describes the typical response of the spring-to-fall ozone ratio to a one-unit increase in the absolute value of 100 hPa meridional heat flux. Since the absolute value of the heat flux is proportional to the upward component of the Eliassen-Palm flux, the slope diagnoses the response

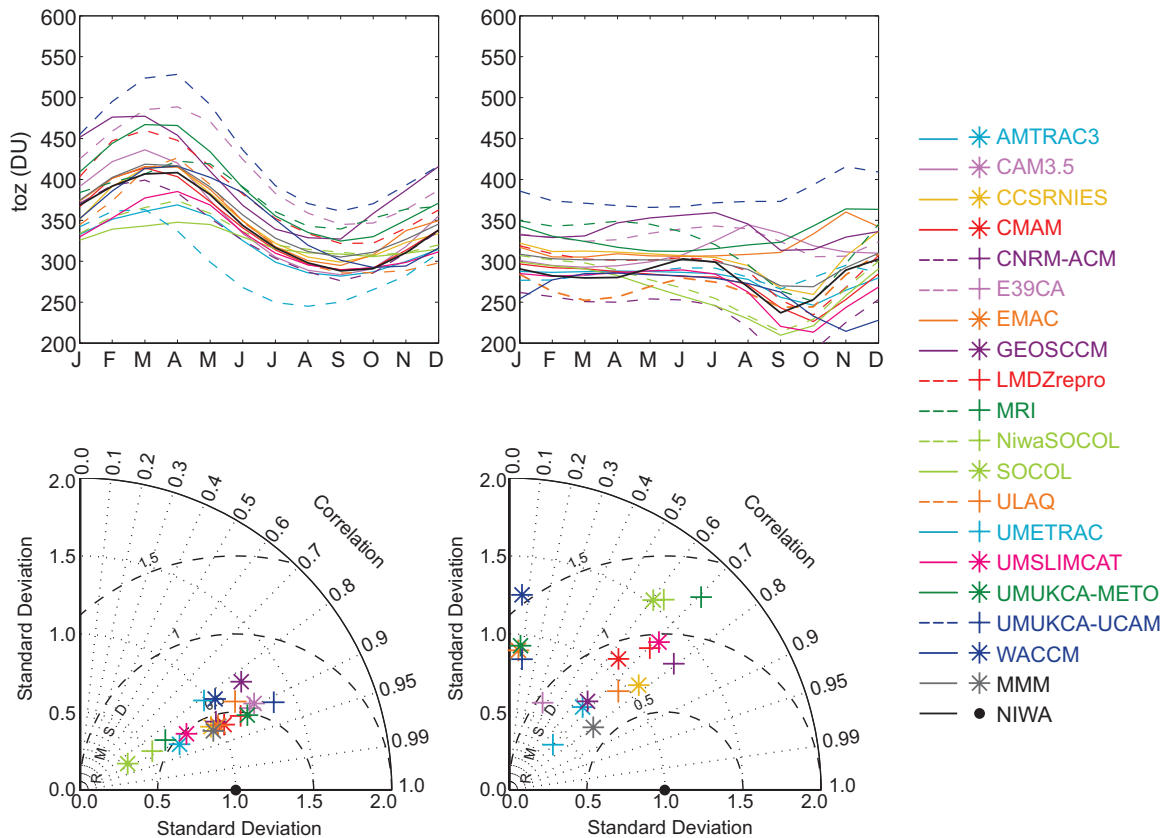


Figure 8.6b: Mean polar cap averaged column ozone (DU, upper panels) and corresponding normalised Taylor diagrams (lower panels) for NH (left) and SH (right) over the period onward of 1980. Legend for model results in the upper panels: Star (cross) symbols correspond to solid (dashed) lines. Black solid line represents NIWA-column data.

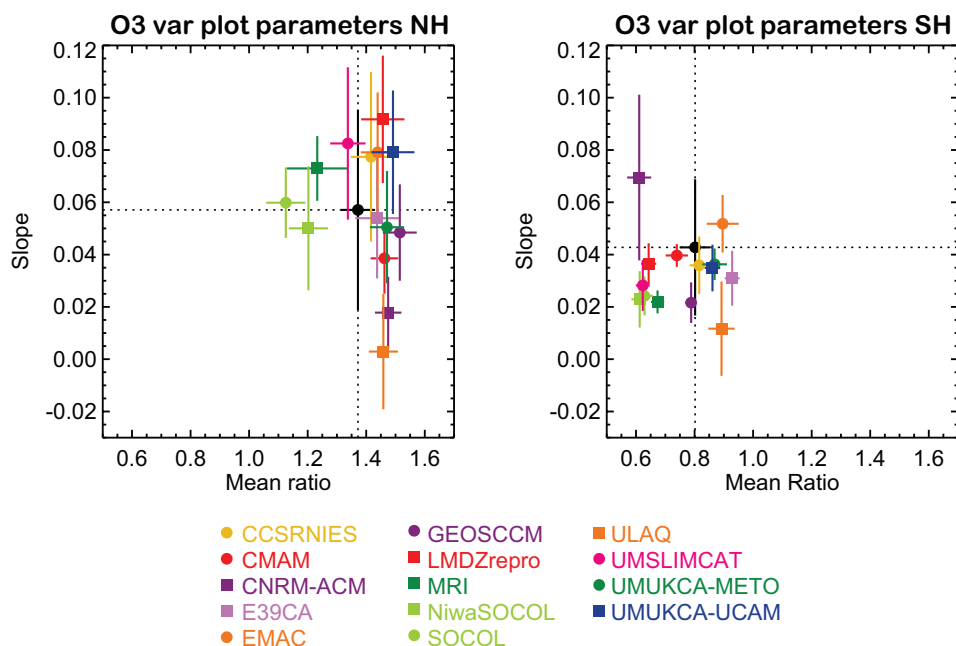


Figure 8.7: Slope parameter ($1/\text{K ms}^{-1}$) of the linear fit to the scatter plots of the Spring/Autumn ozone ratio versus the 100 hPa winter heat flux, plotted against the mean Spring/Autumn ozone ratio for each model. NH (left) and SH (right). Black symbols represent ERA-Interim and NIWA-column data. Each model is plotted with a single coloured dot or square, 95% confidence intervals for the slope parameters are shown in solid lines.

of ozone over each polar cap to changes in the amount of planetary wave activity entering the lower stratosphere. The mean ratio of the spring-to-fall ozone concentration diagnoses the average seasonality in ozone concentrations present in each model. This is a more useful measure of the position of the model on each scatter plot than the intercept of the regression line, which is usually a large distance from the centre of the cloud of points for each model.

Figure 8.7 shows that for most of the models the slope parameter is within the sampling uncertainty of the observations, for both hemispheres. Only the slope parameter of the ULAQ model is indicative of a much weaker relationship (close to zero in the NH) between the heat flux and spring-to-fall ozone ratio, possibly related to the limited horizontal resolution of the ULAQ model. Note that ULAQ is also characterized by a weak relationship between lower stratospheric temperature and heat fluxes, in the NH (Chapter 4). The CNRM-ACM result is for 10 years only so could be different to the rest of the model results for this reason. In the NH (Figure 8.7 left panel), there is a larger spread and a larger uncertainty in the slope parameter than in the SH (right panel), possibly because of the larger NH interannual variability in planetary wave activity (Chapter 4). In the NH, Chapter 4 reports a tendency for enhanced sensitivity in the lower stratospheric polar temperature to the winter heat fluxes. This Chapter 4 result is consistent with the slight overestimation of the ozone sensitivity to the heat flux suggested by the cluster of the model points,

located above the value of the slope parameter of the observations (once CNRM-ACM, because it is based on a shorter data set, and ULAQ, since it is an outlier are excluded). In the SH, most of the models show a smaller inter-model spread and tend to under-estimate the slope parameter. This result is not entirely consistent with the temperature sensitivity reported in Chapter 4, which shows both higher and lower modelled sensitivity of the lower polar stratospheric temperature to the heat fluxes. Concerning the mean spring-to-fall ozone ratio in the models, in the NH the NIWA-column data fall approximately in the middle of the model range. Very weak transport of ozone into the vortex is implied for the MRI, NiwaSOCOL and SOCOL models, explaining the low NH spring time column ozone previously noted. In the SH, there is a relatively large spread in the mean ratio of the September/March column ozone between the models, with about half of the models with smaller or larger ratio than observed (consistent with Figure 8.6b right). Given that the September/March ratio is less than 1.0 because of polar ozone depletion, *i.e.*, the ratio is influenced by chemistry and not just dynamics. This suggests that biases in the modelling of polar chemical processes (Chapter 6) can contribute to this spread in model results. It is also possible that the advection of ozone rich air into the polar cap, which would tend to produce a September/March ratio above 1, is weaker in most models than in the reanalysis, although analysis of some of the same models in Chapter 4 did not suggest that the strength

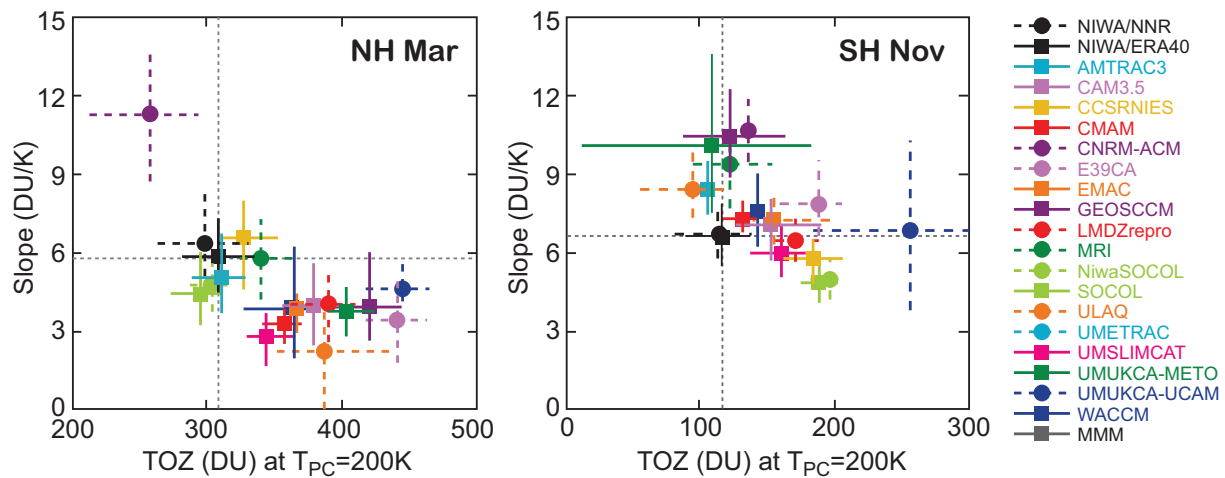


Figure 8.8: Slope parameter (DU/K) of the linear fit to the scatter plots of the polar cap averaged column ozone versus 50 hPa temperature, plotted against the column ozone value of the linear fit at $T = 200$ K for each model. NH (left) and SH (right). Black solid (open) symbols represent NNR (ERA-40) reanalysis and NIWA-column data. Each model is plotted with a single coloured symbol, 95% confidence intervals for the slope parameters are shown in solid or dashed lines.

of their Brewer-Dobson circulation was too weak. There is some indication in Chapter 5 that models with a much lower ratio of September/March ozone in the SH perform poorly in diagnostics of their polar isolation (LMDZrepro, MRI, NiwaSOCOL, SOCOL). However, it is also true that some models with good transport diagnostics also show low spring-to-fall ozone ratios here.

8.4.2 Temperature and column ozone

The tight relationship between heat flux and temperature (Newman *et al.*, 2001, see also Chapter 4) motivates an extension of the analysis presented in Figure 8.7 by evaluating the relationship between column ozone and lower stratospheric temperatures. The existence of such a relationship has previously been identified by Newman and Randel (1988) and Fortuin and Kelder (1996).

In this section, polar cap averaged (60° - 90°) monthly temperatures at 50 hPa are compared against polar cap averaged total column ozone. The analysis is focused on spring (March for the NH and November for the SH), which is the time when the cumulative effects of wave activity during the previous winter on ozone and temperature are most pronounced. The analysis is performed for every year of model data from 1960 to the end of each simulation and for the common periods between the NIWA-column ozone and, respectively, the NCEP/NCAR reanalysis (hereafter: NNR, updated from Kalnay *et al.*, 1996) and the ERA-40 reanalysis.

Figure 8.8 displays the slope parameter of the linear fit between column ozone and temperature and its 95% confidence intervals. The slope parameter indicates how

sensitive column ozone is to a given temperature perturbation. On the x-axis is reported the ozone amount of the linear fit at a temperature of 200 K, which is used as a second parameter to describe the goodness of the fits.

The results shown in Figure 8.8 indicate that the models perform adequately over both polar caps, in the sense that all slopes are positive showing that column ozone increases when temperatures are anomalously warm. However, for the NH (March, left panel), only 5 models (AMTRAC3, CCSRNIES, MRI, NiwaSOCOL, SOCOL) reproduce the observed relationship reasonably well. UMUKCA-UCAM does not under-estimate the slope significantly, but has a large amount of ozone at the temperature of 200 K. One model (CNRM-ACM) considerably overestimates the observed slope. The rest of the models under-estimate the slope up to a factor of two, indicating that for most models the simulated ozone is less sensitive to a given temperature perturbation than in the observations. In November (SH, right panel), the number of models that either over- or under-estimate the observed slope is quite evenly distributed around the observations. The slope is overestimated for CNRM-ACM, GEOSCCM, MRI, and UMUKCA-METO.

Figure 8.8 also indicates that the x-axis values, the amount of ozone at a temperature of 200 K, are too large for most models. This is consistent with the column ozone systematic bias seen in Figure 8.6b. The positive ozone bias is particularly large for the UMUKCA-UCAM model in November, and consequently this model stands out in the SH plot.

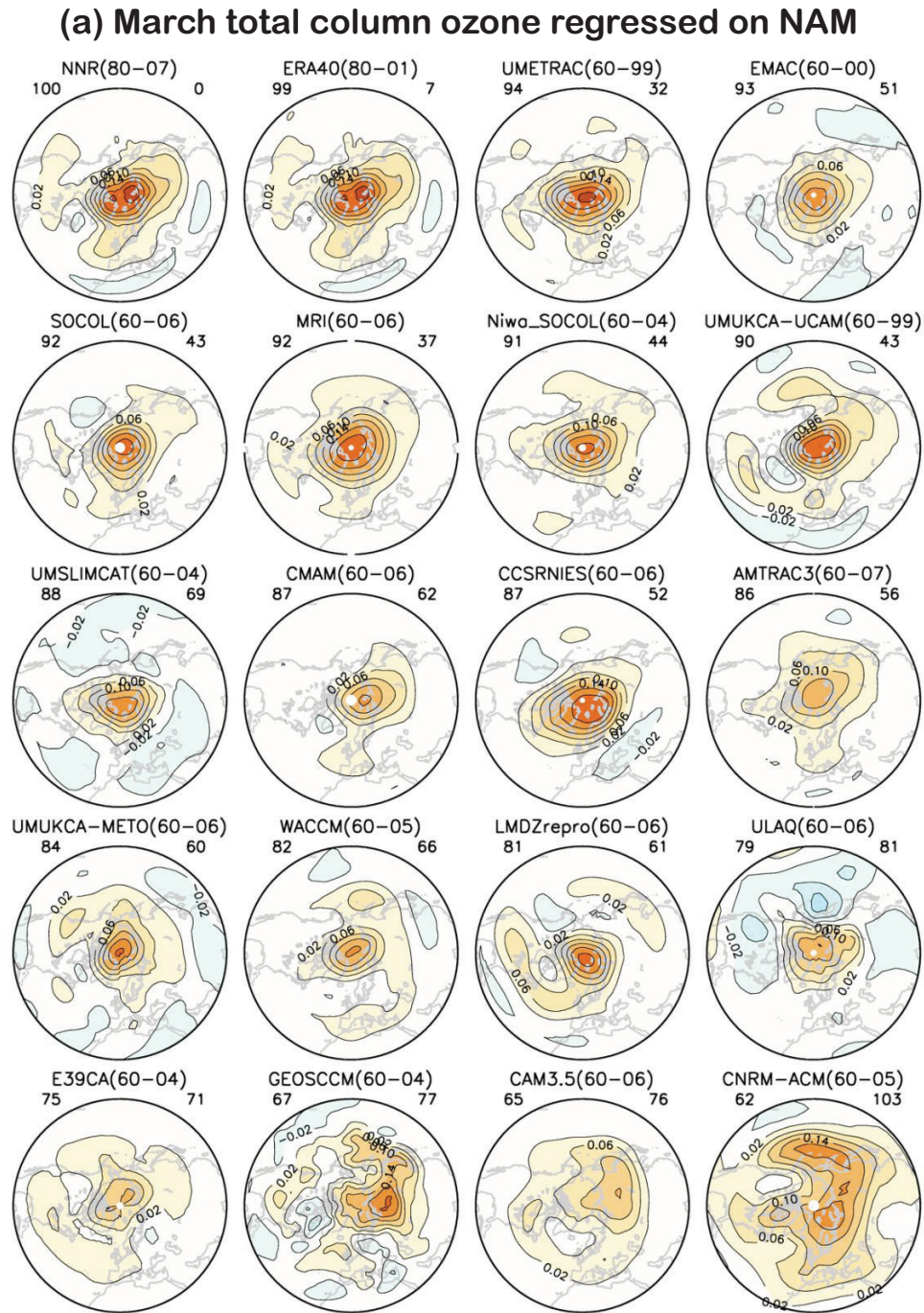


Figure 8.9a: Regression of column ozone on the simplified annular mode for NH March. Contour interval is 0.04 DU/gpm. The numbers on top of each map represent (left) pattern correlations ($\times 100$) and (right) nrms-errors ($\times 100$) between results from the individual models and those from the NIWA-column and NNR. Numbers in parenthesis indicate the period (years) included in the calculations.

8.4.3 Stratospheric annular mode and column ozone

On interannual time scales the strength of the annular mode in the lower stratosphere and the heat fluxes at 100 hPa are closely connected (Hu and Tung, 2002). Therefore,

a relationship should also exist between the column ozone variation and the annular mode. This possibility is investigated by regressing the monthly mean column ozone time series on to a relatively simple definition of the annular mode (AM) index at 50 hPa. The 50 hPa level is chosen because column ozone is mostly affected by variations in the

(b) Nov total column ozone regressed on SAM

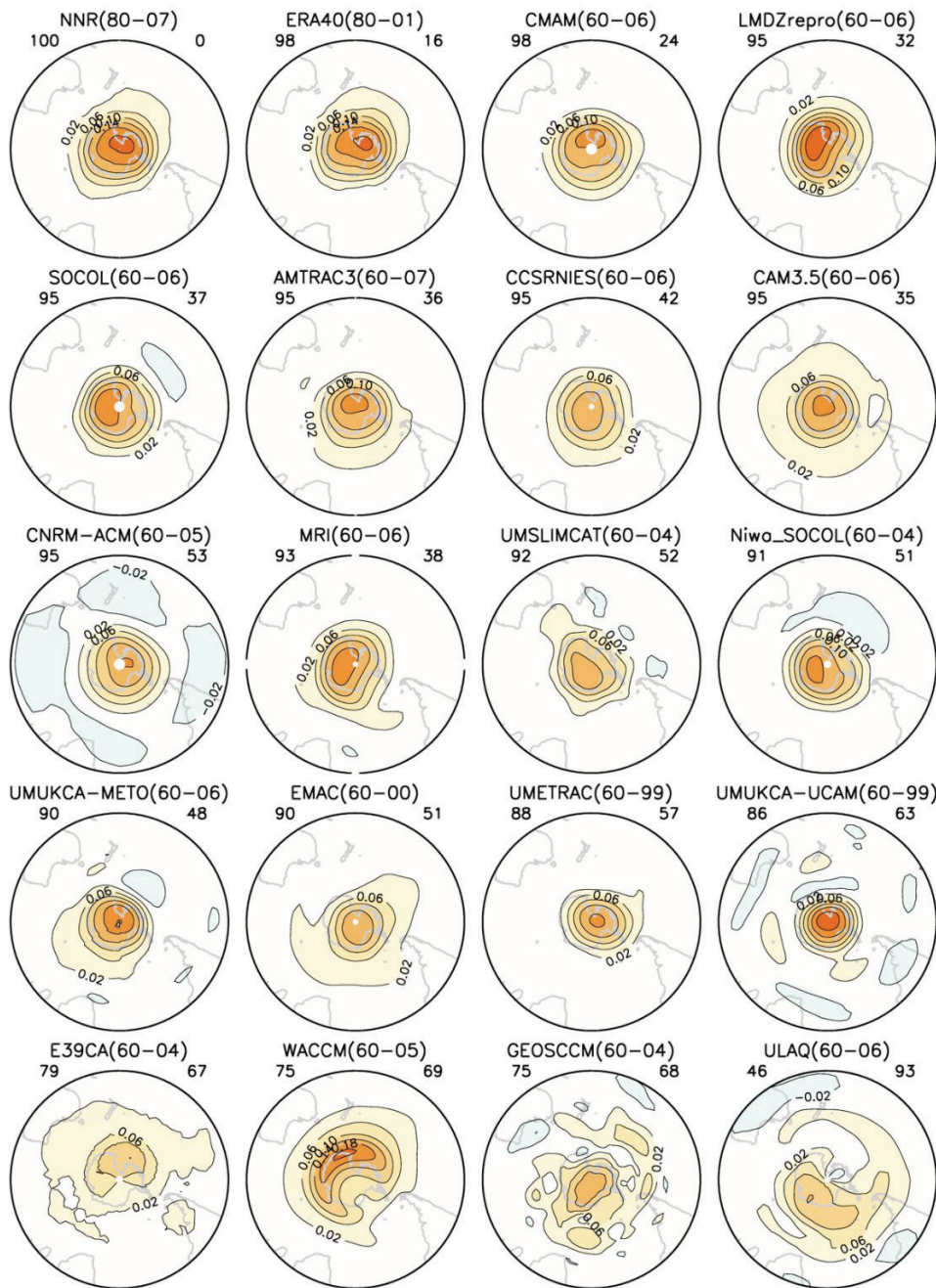


Figure 8.9b: Regression of column ozone on the simplified annular mode for SH November. Contour interval is 0.04 DU/gpm. The numbers on top of each map represent (left) pattern correlations (x100) and (right) rms-errors (x100) between results from the individual models and those from the NIWA-column and NNR. Numbers in parenthesis indicate the period (years) included in the calculations.

lower stratosphere. The simple AM definition is based on polar cap averages (60°-90°) of monthly mean zonal mean geopotential height anomalies at 50 hPa, and is a good approximation of the traditional AM index (Baldwin and Thompson 2009). The simple AM is employed, because it represents an absolute measure and thus avoids possible

ambiguities associated with the polarity and magnitude of the EOF-based approach. Note that, however, it has the opposite polarity from the EOF-based AM. Prior to the analysis, all data are de-trended as previously done for Figure 8.6a. Concerning the observations, the NIWA-column ozone data are used and the AM index is derived from the

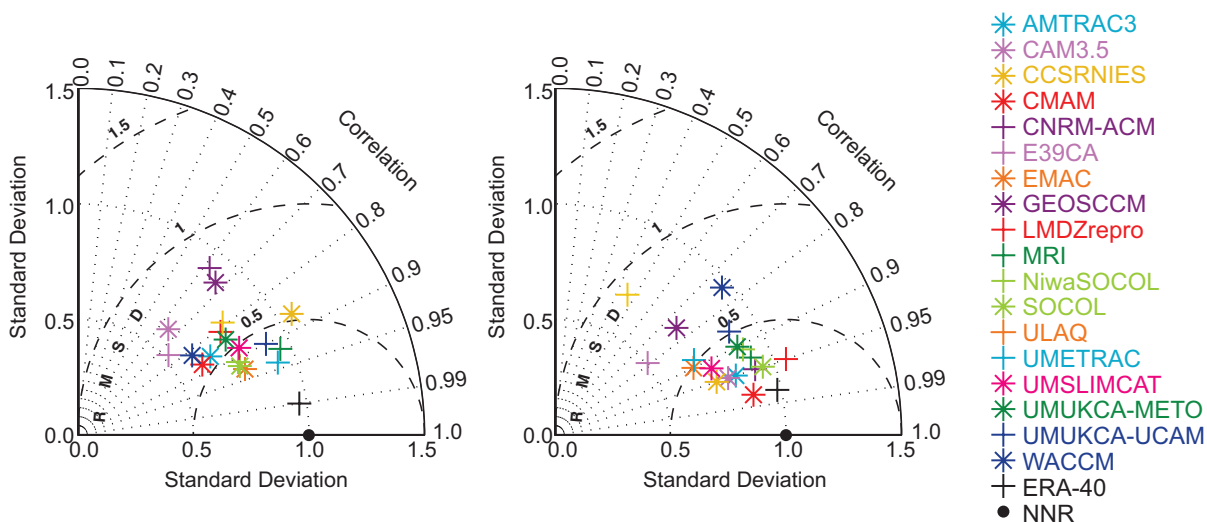


Figure 8.10: Normalised Taylor diagrams of the regression of column ozone on the simplified annular mode for NH March (at left) and SH November (at right). The corresponding fields are shown in Figure 8.9a and 8.9b, respectively.

NNR or the ERA-40 reanalysis, as in Section 8.4.2.

The regression coefficients between local variations of column ozone and the AM index for each model and observations are shown for NH March in **Figure 8.9a** and for SH November in **Figure 8.9b**, the dynamically active seasons (section 8.4.1) and a time when this relationship is expected to be robust. The corresponding Taylor diagrams quantifying model performance with respect to NIWA/NNR are shown in **Figure 8.10**. Therefore, **Figure 8.10** (left) evaluates the longitude-latitude pattern of the modelled ozone versus annular mode regression for NH March, and **Figure 8.10** (right) the one for SH November. As expected, using the simple AM leads to positive regressions over the polar regions. Column ozone is high when the AM is positive, *i.e.*, when the geopotential height anomalies over the pole are positive, indicative of a warm and weak vortex, increased wave activity, and an anomalously strong descending branch of the Brewer-Dobson circulation at polar latitudes.

Figure 8.10 (left) shows that for NH March, most models reproduce the basic structure of the observed regression patterns in the sense that most models have a correlation coefficient with NIWA/NNR larger than 0.7. The three outliers (CAM3.5, CNRM-ACM, and GEOSCCM) still have relatively high correlations larger than 0.6. The amplitude of the observed regression pattern is less well simulated, with most of the models tending to underestimate it (standard deviation less than 1).

In the SH, **Figure 8.10** (right) shows a better simulation of the observed pattern for SH November. In this case, the outlier is ULAQ, because of its very small correlation (smaller than 0.5), while E39CA, GEOSCCM, and WACCM have correlations between 0.7 and 0.8, and the rest of the models have correlations close to or higher

than 0.9. The decrease in the spread of the model results is due to the improvement in the structure of the modelled regression pattern, while the performance in its amplitude (measured by the standard deviation) is comparable in the two hemispheres. Possibly, the better simulation of the structure of the regression pattern in the SH is related to the more zonal character of the large scale stratospheric dynamics there.

8.5 Solar Cycle

The 11-year solar cycle has a direct impact on ozone *via* radiation and chemistry in the upper stratosphere and indirect effects on dynamics, transport and chemistry throughout the stratosphere (*e.g.*, review by Gray *et al.*, 2010). The direct effect in the upper stratosphere depends on a good representation of solar radiation processes in both the radiative transfer and in the photochemistry parameterisations (see Chapters 3 and 6 for a comparison of radiation codes and photochemical schemes respectively). These were reasonably well simulated by the CCMVal-1 models (Austin *et al.*, 2008). However, the indirect dynamical effects in the tropical lower stratosphere and extra-tropical stratosphere and the extension of the signal into the troposphere (see *e.g.*, Haigh, 1999; Kodera and Kuroda, 2002; Matthes *et al.*, 2004; Haigh *et al.*, 2005; Kodera, 2006; Matthes *et al.*, 2006; Gray *et al.*, 2010) are more challenging to reproduce. Matthes *et al.* (2003) suggested that a realistic representation of the model's climatology is an important pre-requisite for reproducing the indirect dynamical effects. Other suggested important "ingredients" are a QBO, time-varying solar irradiances, and realistic interannual variability in the SSTs. Another

remaining challenging task is to understand the observed modulation of the solar signal with the tropical oscillations (QBO and SAO) at the equatorial as well as at the high-latitude stratosphere (see *e.g.*, Labitzke, 1987; Labitzke and van Loon, 1988; Gray *et al.*, 2001). This interaction is still difficult to investigate since the number of observed events when separated into solar and QBO phases is small and only some of the CCMs reproduce an internally generated QBO, a prerequisite to study the full solar/QBO interaction. On the other hand there is still considerable uncertainty in the observed solar cycle signal, so an understanding of the modelled responses might help to understand the observed response. In the following section the solar cycle response is examined without considering the more complicated tropospheric responses and extra-tropical interactions, which are beyond the scope of the current report.

Five models (GEOSCCM, ULAQ, UMECTRAC, UMUKCA-METO, UMUKCA-UCAM; referred to as the non-sc group) do not prescribe a solar cycle in irradiances and are therefore not included in the following analysis. **Table 8.3** shows a comparison of the solar regression coefficients from the MLR in total column ozone from 60°S to 60°N compared with the observed solar regression coefficient from the NIWA total column ozone data set. While the models from the non-sc group consistently show a solar regression coefficient around zero, most of the models that impose a solar cycle show a solar regression coefficient that is 70% to 80% of the observed value. WACCM, MRI, and UMSLIMCAT show the best agreement with the observed values, while CAM3.5 is biased low and CCSRNIES and CNRM-ACM are biased high. These high biases in CCSRNIES and CNRM-ACM may be related to biases in their ozone climatologies (*e.g.*, Figures 8.2-8.5). Differences in the radiation schemes and the input data (either spectrally resolved solar UV data and/or total solar irradiance (TSI) data) are discussed in Chapter 3, Section 3.6. The difference between the two low-top models E39CA and CAM3.5 that do not include the whole stratosphere is surprising. While CAM3.5 shows a 53% correspondence with observations, a value that might be expected from a low top model, E39CA performs very well (82%). Note also that there are substantial uncertainties from observations. While only the NIWA-column estimate is shown in comparison with the models, Randel *et al.* (2007, Figure 12) showed a factor of two difference among TOMS, SBUV, SAGE, and ground-based estimates.

8.5.1 Vertical structure of temperature and ozone signal in the tropics

Considerable discrepancies exist between the various observational estimates of the vertical structure of the tropical solar signal (Gray *et al.*, 2010) as well as between observations and models (WMO, 2007), especially be-

low 10 hPa. Austin *et al.* (2007; 2008) showed that recent model studies have achieved an improved vertical structure in this region and speculated that it may be related to (a) the introduction of time-varying solar cycle irradiances instead of the constant solar min/max simulations that had previously been performed because of limited computer resources or (b) an aliasing effect of the SSTs with the solar cycle. Marsh and Garcia (2007) discuss the inability of the MLR technique to take into account autocorrelation between *e.g.*, the solar and the ENSO signal, although the MLR analysis employed here should be able to handle this since the autocorrelation in the residual is taken into account (*e.g.*, Crooks and Gray, 2005). Nevertheless, the real atmosphere is highly non-linear and it may be difficult to capture the solar signal completely with the linear method used here. Another factor that complicates the solar signal is the QBO. Lee and Smith (2003) and Smith and Matthes (2008) discuss an aliasing effect of the QBO (and volcanoes) with the solar cycle. Frame and Gray (2010) have recently demonstrated that the volcanic influence is unlikely to be important. Recently, Matthes *et al.* (2010) showed that in their model the observed vertical structure in the tropical solar ozone and temperature signal in the middle and lower stratosphere can be reproduced only when a QBO is present.

Figure 8.11 shows the annual mean of the tropical vertical solar signal in temperature and ozone from the

Table 8.3: Solar regression coefficient for total column ozone from 60°S to 60°N for the CCMs that impose a solar cycle compared to observations (NIWA-column).

CCM	Solar regression coefficient/100 units of F10.7 cm solar flux	%
AMTRAC3	2.8	74
CAM3.5	2.0	53
CCSRNIES	6.5	171
CMAM	3.2	84
CNRM-ACM	7.3	192
E39CA	3.1	82
EMAC	2.7	71
LMDZrepro	2.9	76
MRI	4.1	108
NiwaSOCOL	2.7	71
SOCOL	2.8	74
UMSLIMCAT	3.4	89
WACCM	3.8	100
observations NIWA column	3.8	-

MLR analyses. The relative uncertainties have been calculated by dividing the uncertainty from the MLR (square root of the sum of the squares of the diagonal elements in the covariance matrix) by the solar regression coefficient and normalising it. Therefore, relative uncertainty values below one indicate statistically significant results. The largest and statistically significant temperature and ozone solar response occurs in the upper stratosphere around 1 and 3 hPa, respectively. This is the direct solar effect due to enhanced UV absorption during solar maxima that leads to higher temperature and greater ozone production, which in turn increases the temperature. Most of the models produce a temperature response of about 0.6 K per 100 units of the F10.7 cm radio flux (multiply with 1.3 to get the difference between solar maximum and minimum of the solar cycle) around the stratopause, although the values range

from up to 1.1 K in CNRM-ACM, 0.9 K in WACCM, down to ~ 0.35 K in LMDZrepro and SOCOL. Note that UMSLIMCAT shows a larger warming of about 1 K higher up near 0.3 hPa. The majority of the modelled temperature responses in the upper stratosphere are similar to the SSU observations, although the ERA-40 data show a slightly larger temperature signal of 1.3 K.

The modelled temperature responses are consistent with the shortwave heating rate responses shown in **Figure 8.12**. Models with the largest differences of about 0.15 K/day (EMAC, WACCM, CMAM, CCSRNIES) produce the largest temperature responses around the stratopause. However, even though MRI has the largest shortwave heating rate difference, it does not show an especially large temperature response. The results are also consistent with the offline solar radiation calculation results in Chapter

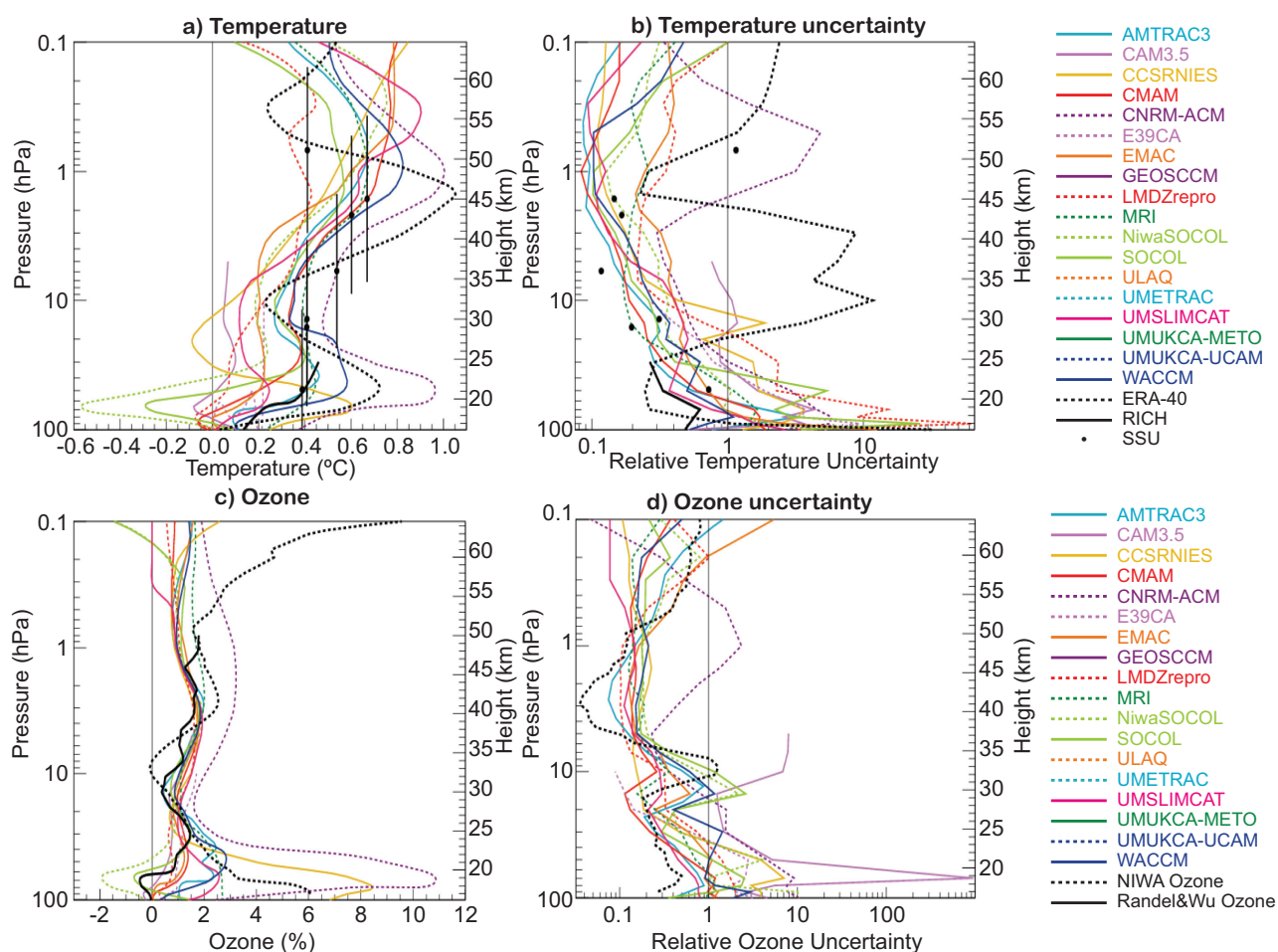


Figure 8.11: Annual mean tropical (25°S - 25°N) solar regression coefficients for (a) temperature in Kelvin per 100 units of the F10.7cm radio flux, (b) the relative uncertainty (uncertainty from MLR divided by the regression coefficient and normalised) temperature, (c) ozone in %/100 F10.7cm units, and (d) the relative uncertainty in ozone. From CCMVal-2 CCMs (1960-2004) and observations (NIWA-3D ozone, 1979-2004, Randel&Wu ozone (1979-2005), RICH radiosonde data (1960-2004), ERA-40 (1979-2001), and SSU data (1979-2005)) from 100 to 0.1 hPa. Note that the Randel&Wu ozone data are displayed in DU/km, whereas the CCMs and the NIWA-3D ozone data are on pressure levels.

3 (although note that the offline radiation calculations in Chapter 3 do not necessarily correspond to model results in Figure 8.12; *e.g.*, UMUKCA-UCAM does not have a solar cycle in the REF-B1 simulation and is therefore in the non-sc group in this chapter, although it shows shortwave heating rate differences from the offline radiation calculations in Section 3.6 that are related to solar induced ozone changes in the offline calculations only). LMDZrepro only prescribes total solar irradiance changes, so under-estimates the shortwave heating (Figure 8.12) and therefore the solar temperature response (Figure 8.11). Some of the models with large shortwave heating response (MRI and EMAC in Figure 8.12) show smaller temperature signals (Figure 8.11) than models with smaller shortwave heating responses (*e.g.*, WACCM). In summary, the solar induced temperature responses in Figure 8.11 are produced by a combination of solar UV radiation changes and solar induced ozone changes, which depend both on the prescription of spectrally resolved or total solar irradiance changes in the radiation and on the photochemical schemes and their individual performances (see Chapters 3 and 6).

Discrepancies between the models themselves and with the observations increase below 10 hPa consistent with larger relative uncertainties (Figure 8.11b). Some CCMs show a positive solar temperature signal (Figure 8.11a) that increases with increasing height in good agreement with the SSU data, whereas others such as AMTRAC3, WACCM, SOCOL, CCSRNIES and EMAC show a relative minimum in the middle stratosphere like the ERA-40 data although the height of their respective minima differs. Some models (AMTRAC3, CMAM, CNRM-ACM, CCSRNIES, MRI, and WACCM), show a distinct secondary temperature maximum in the lower stratosphere, which

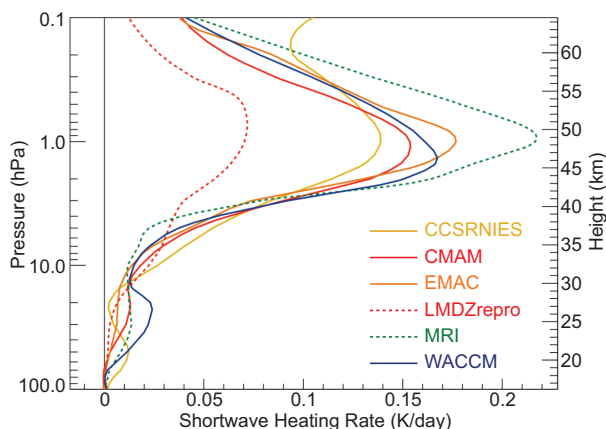


Figure 8.12: Solar cycle shortwave heating rate differences in Kelvin per day in 100 units of the F10.7cm solar flux (multiply by 1.3 to obtain the difference between solar maximum and solar minimum) averaged between 25°S and 25°N for those CCMs that prescribed a solar cycle and provided data.

is also present in the RICH radiosonde data (0.4-0.5 K) and the ERA-40 data (~0.7 K). But as noted above these changes are not statistically significant.

The vertical structure of the solar signal in ozone is much better represented in the models compared to observations, than in the case for temperature (Figure 8.11c). The models compare well with the Randel&Wu ozone data in the middle and upper stratosphere while the agreement between the models, and between the models and observations, deteriorates in the lower stratosphere due to the increased uncertainties (Figure 8.11d). The NIWA-3D data set shows a clear upper stratospheric maximum, a minimum in the middle stratosphere, and a secondary maximum in the lower stratosphere. A secondary peak in ozone in the lower stratosphere between 20 and 25 km, a region where the largest ozone column changes occur, is simulated by AMTRAC3, CNRM-ACM, CCSRNIES, MRI, and WACCM. Except for AMTRAC3 and CNRM-ACM these models have variability related to a (prescribed) or internally generated QBO-like oscillation. Similar to the temperature response, the ozone response and its uncertainties in the lower stratosphere for CCSRNIES and CNRM-ACM are very large compared to the other models and observations. These models were also outliers in the ozone climatology inter-comparison (Figure 8.3), CCSRNIES was graded low for nearly all photolysis rates in the PhotoComp inter-comparison (Chapter 6), and both models showed very fast tropical ascent rates in the transport comparison (Chapter 5).

Note that both low-top CCMs (CAM3.5 and E39CA) produce only a small solar signal in temperature since they do not include the stratopause region where the initial solar signal appears. CAM3.5 produces a similarly small signal in ozone, whereas E39CA shows a relative large solar ozone signal consistent with the largest signal in column ozone in Table 8.3.

8.5.2 Latitudinal structure of the solar signal in temperature and ozone

The latitudinal structure of the amplitude of the solar cycle in temperature and ozone is shown in **Figure 8.13** at 1 and 3 hPa, respectively. Apparent is the large spread of model results which is larger for temperature than for ozone. The modelled solar signals in ozone are similar in the tropics and mid-latitudes while large differences occur at northern and southern high latitudes due to large interannual variability (see Section 8.4). The models agree well with the Randel&Wu data but are lower than the NIWA-3D solar ozone signal in the tropics. EMAC and WACCM show the largest latitudinal variations; in the SH this agrees well with the NIWA-3D ozone. Again, CNRM-ACM is biased high from 60°S to 60°N.

The solar temperature signal shows more variabil-

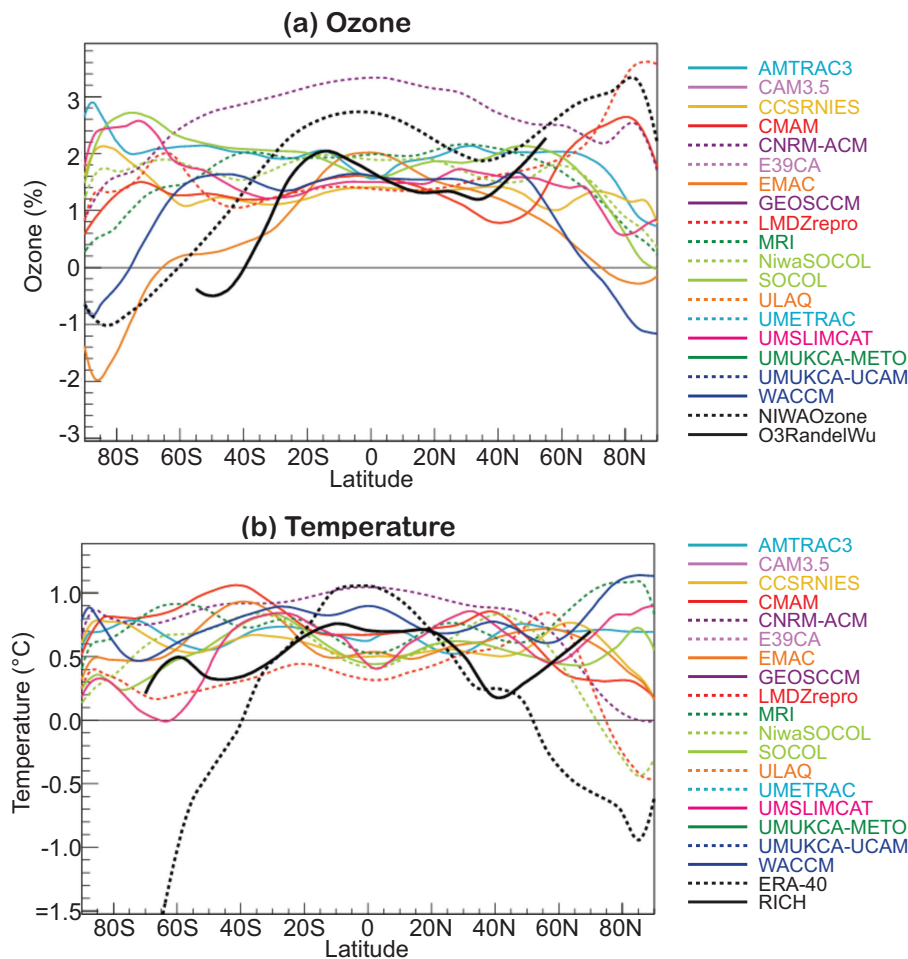


Figure 8.13: Amplitude of the solar cycle in the upper stratosphere over latitude for ozone at 3 hPa in %/100 units of the F10.7cm radio flux (top) and temperature at 1 hPa in K/100 units of the F10.7 cm radio flux (bottom). Note that the Randel&Wu data represents the 40 km height values, and the SSU data the 45 km values.

ity between the CCMs than the ozone signal. Most models show a relatively flat response of about 0.5 K between 60°S and 60°N. The ERA-40 response, on the other hand, shows a peak response at equatorial latitudes and decreases to higher latitudes. As with the ozone data sets, there is significant variation between the different observational data sets (Gray *et al.*, 2010). However, neither observational data set demonstrates statistical significance poleward of ~30°, so validation of the models at these latitudes is difficult. The difficulty of reproducing the latitudinal structure of the solar signal is also apparent in the latitudinal structure of the annual-mean solar regression coefficient for column ozone (see supplementary material, Figure S8.8). The spread in model responses is especially large at high northern latitudes due to dynamical interactions. Very large deviations are seen for EMAC and WACCM at high latitudes. These differences might be related to differences in the transport schemes, because transport and dynamical processes in lower stratospheric ozone dominate the distribution of column ozone variations. Both models have a

large cold bias in the SH (Chapter 4) and too low Cl_y in the vortex. In addition, WACCM has too much mixing in the TLS and EMAC has subtropical and polar lower stratospheric barriers that are too weak (Chapter 5).

Since the spread in both the modelled and observed solar cycle signal is so large, especially at high latitudes, no further diagnostics are presented to investigate dynamical feedback mechanisms (Kodera and Kuroda, 2002), such as those shown by Matthes *et al.* (2003) who investigated GCMs in which the ozone solar signal was imposed. Recent model studies (*e.g.*, Matthes *et al.*, 2006; Gray *et al.*, 2006; Ito *et al.*, 2009; Matthes *et al.*, 2010) suggest that these dynamical feedback mechanisms are particularly difficult to reproduce, because of possible non-linear interaction with the QBO, and are currently best investigated in more idealised model studies in which the various influences can be examined separately.

Several studies have highlighted the limitations of the MLR analysis with respect to the time period chosen and the difficulty of separating autocorrelated signals such as

the solar and the QBO, volcanic or ENSO signal in the equatorial lower stratosphere (*e.g.*, Smith and Matthes, 2008; Marsh and Garcia, 2007; Austin *et al.*, 2008; Frame and Gray, 2010). The sensitivity of the MLR analysis presented here has been tested using different time periods, *i.e.*, 1960-2004 and 1979-2004. The details of the results are not very sensitive to the period chosen, apart from the magnitude of the response changes, which is larger for the shorter time period. This allows confidence in the performance of the MLR method, provided careful representation is made of all possible basis functions as well as an auto-correlation of the residuals.

8.6 QBO in Ozone

In the tropical stratosphere, the QBO in zonal wind is a major driver of ozone variability (see Baldwin *et al.*, 2001). Typically, however, general circulation models of the atmosphere have difficulties in spontaneously simulating the QBO. In order to simulate a realistic QBO, a model should be able to support a realistic spectrum (temporal and spatial) of upward propagating waves in the tropics. This is a major challenge, because this spectrum of waves depends on many technical aspects of an atmospheric general circulation model, such as tropical convection parameterisation, stability of the troposphere, SSTs, vertical and horizontal resolutions and atmospheric gravity wave parameterizations (*e.g.*, Scaife *et al.*, 2000; Giorgetta *et al.*, 2002, 2006; Shibata and Deushi, 2005).

A model that does not appropriately simulate the QBO in zonal wind, also severely misrepresents the natural ozone variations associated with the QBO (Punge and Giorgetta, 2008). Therefore some modelling groups have imposed the QBO by assimilation techniques (*i.e.*, nudg-

Table 8.4: Tropical variability in the CCMVal-2 models. Models in Group A and Group B do not assimilate the QBO. Models in Group C assimilate the QBO (via nudging of the zonal winds or vorticity). Group A models have basis functions in the MLR analysis set to zero. Models in Group B and C are included in the MLR analysis.

GROUP A	GROUP B	GROUP C
CMAM	AMTRAC3	CAM3.5
CNRM-ACM	MRI	CCSRNIES
GEOSCCM	UMETRAC	E39CA
LMDZrepro	UMUKCA-METO	EMAC
	UMUKCA-UCAM	NiwaSOCOL
	UMSLIMCAT	SOCOL
		ULAQ
		WACCM

ing, see Chapter 2) of either the equatorial zonal winds or the vorticity. The models that assimilate the QBO in the REF-B1 simulation are shown in Chapter 2 (Table 2.8), and referred to as Group C in **Table 8.4**. Although the assimilation of the QBO should alleviate the biases in the ozone distribution associated with the problem of properly representing the QBO, it unfortunately removes the predictive capability of a model. While it is therefore possible to evaluate the response of ozone to a prescribed QBO forcing, a prediction of future ozone behaviour related to the QBO is impossible with this methodology.

8.6.1 Equatorial Variability and the QBO signal in the stratosphere

Figure 8.14 shows the vertical profile of the variability of zonal-mean zonal wind (left) and ozone in DU/km (right) at the Equator (average 5°S-5°N) computed as the standard deviation of the monthly values for the period 1960-1999. In both model and observational data, the linear trend and the annual cycle have been removed. In addition, a band pass filter has been applied to the time series to extract only those oscillations with periods between 9-48 months. The upper panels include only the models with nudged QBO (Group C of Table 8.4), while the bottom panels include the rest of the models (both Groups A and B of Table 8.4).

The models in Group C are characterized by substantial variability, from ~10 m/s up to ~18 m/s in zonal-mean zonal wind and in the range 0.7 to 1.5 DU/km in ozone, as expected because of the assimilation. In addition to the main peak near 20 hPa in zonal-mean zonal wind, some models (NiwaSOCOL, SOCOL, and to a lesser extent WACCM) show a secondary peak in zonal wind variability near 1 hPa. This variability could be excessive QBO modulation of the SAO at these altitudes, a possible side effect of the applied nudging.

In the models that did not assimilate the QBO (lower panels), the zonal wind variability clusters into two groups: 4 models (GEOSCCM, LMDZrepro, CNRM-ACM, and CMAM) have variability less than 5 m/s (Group A); and 6 models (AMTRAC3, MRI, UMETRAC, UMUKCA-METO, UMUKCA-UCAM, and UMSLIMCAT) have variability in the range 7 to 22 m/s (Group B). Group A severely under-estimates the zonal wind variability, leading to the conclusion that the QBO in zonal wind is not internally generated to a sufficient degree in these models. For consistency in these models the QBO basis functions in the MLR analysis are set to zero (see Table 8.4). The variability in Group B is much more realistic when compared with ERA-40 reanalysis, although the maximum amplitude is both overestimated (UMETRAC and UMSLIMCAT) and under-estimated (AMTRAC3, MRI, UMUKCA-METO, UMUKCA-UCAM) and tends to be located at lower pres-

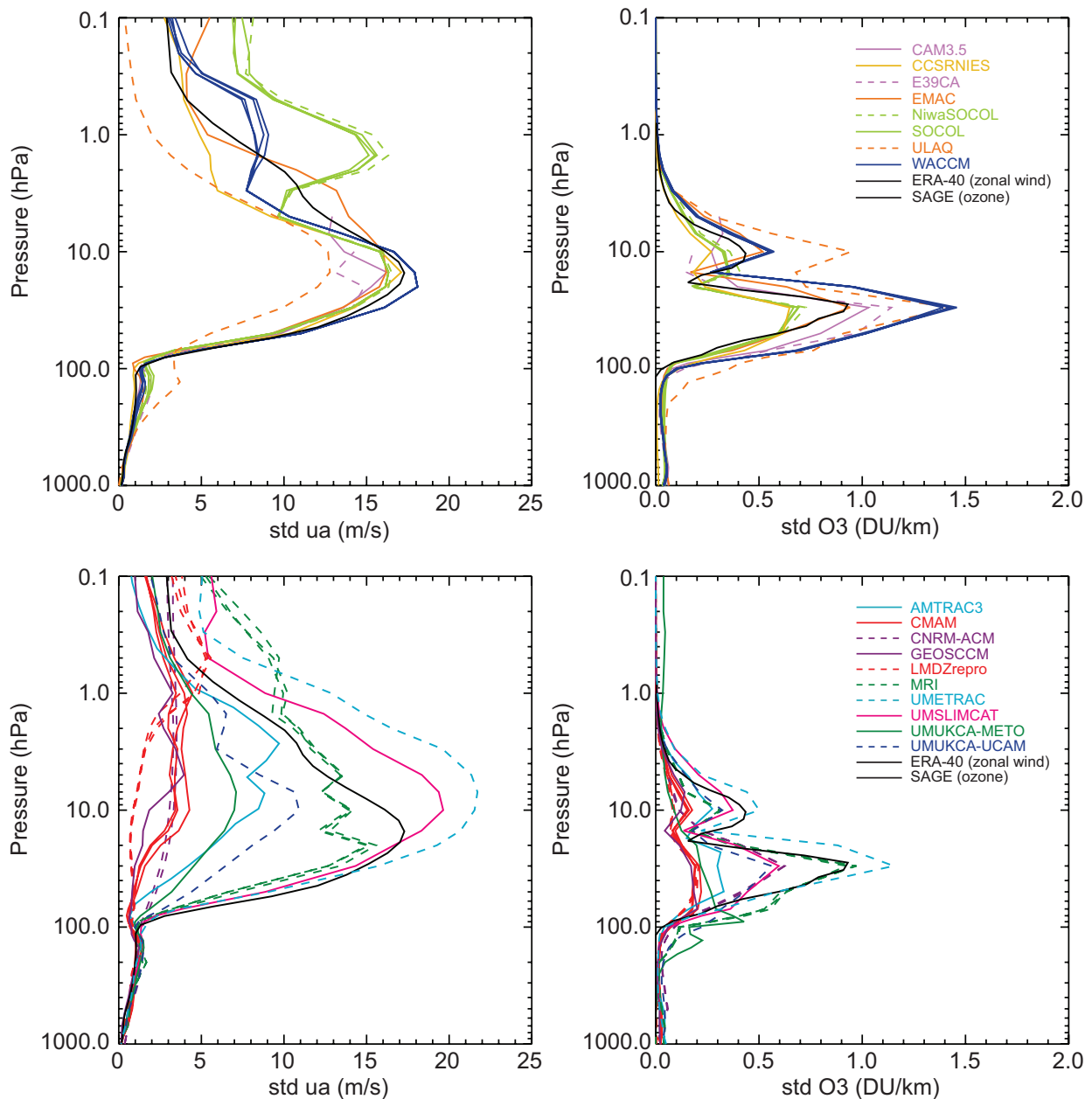


Figure 8.14: Monthly zonal-mean standard deviation of zonal-mean zonal wind (left, m/s) and ozone (right, DU/km) averaged from 5°S to 5°N. Results from the CCMVal-2 CCMs (in colour), ERA-40 (left, black), and SAGE data (right, black). From de-trended, de-seasonalised and filtered (9–48 months) time series. Top panels: Group C CCMs, bottom panels: Groups A and B CCMs.

sure (*i.e.*, higher in the atmosphere) than observed.

The observed interannual variability of ozone (right panels) shows two maxima (10 and 30 hPa). These maxima are due to the modulation of the ozone chemistry in the middle stratosphere (10 hPa, see Chapter 6) and the advection of ozone by the secondary meridional circulation (30 hPa, see Chapter 5) in the lower stratosphere (Gray and Chipperfield 1990). The models with a nudged QBO (Group C, upper right panel) show the clear double peak structure, in phase with the Randel&Wu observations, al-

though with a wide range of magnitudes. The models without QBO nudging (lower panel) that showed little variance in wind at the equator also simulate little variance in ozone (Group A). The exception in Group A is the CNRM-ACM model, with a 0.6 DU/km peak in ozone variability at 30 hPa. The time series of the ozone vertical distribution is shown in the supplementary material (Figure S8.9) for CNRM-ACM. It shows that these variations are not downward propagating, consistent with the fact that this model does not simulate the QBO. Possibly, these variations are

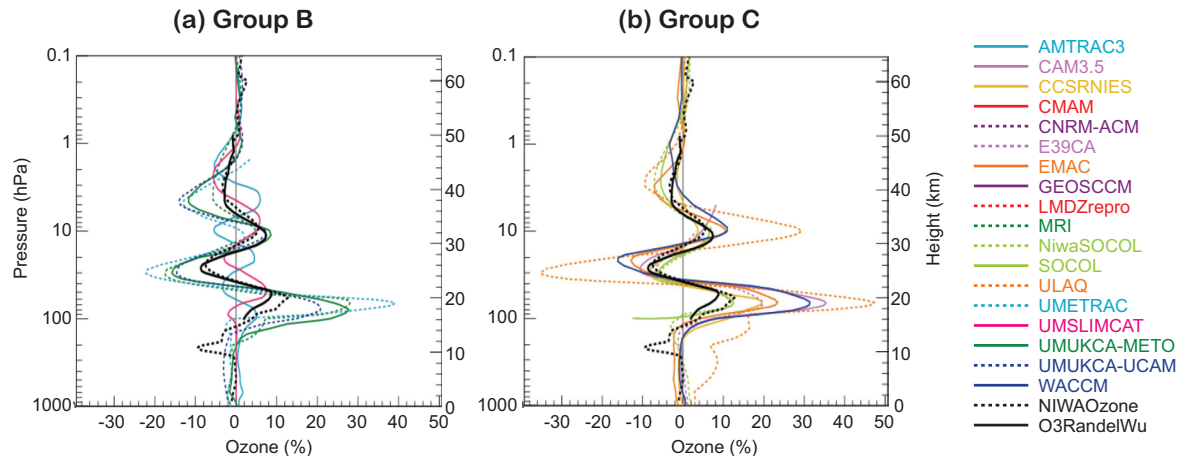


Figure 8.15: Annual mean QBO regression coefficient (multiplied by 30 m/s) in ozone in percent at equatorial latitudes (5°S-5°N) from the CCMVal-2 CCMs (1960-2004) and observations (NIWA-3D ozone, 1979-2004; Randel&Wu ozone, 1979-2005). (a) Group B CCMs. (b) Group C CCMs.

associated with ENSO, which can still be present in the applied band pass filter (9-48 months). A similar behaviour was previously reported for a CCMVal-1 model (Punge and Giorgetta, 2008). With the exception of UМУKCA-METO, the models in Group B show the double peak in ozone variability, each of them to a different degree.

Apart from this very broad comparison, there does not seem to be a linear relationship between the variability in zonal winds and ozone in Groups B and C, suggesting a range of sensitivity of the ozone to the zonal wind QBO, which is independent of whether it is imposed or internally generated. In particular, in Group B the UMSLIMCAT model appears to be characterized by low ozone sensitivity, given its higher than observed wind variability but half than observed ozone variability at 30 hPa. In Group C, the ULAQ and WACCM models appear to have a higher than observed ozone sensitivity, while the NiwaSOCOL and SOCOL sensitivity is lower than observed. Note that the two SOCOL models and WACCM are very close to obser-

vations in their zonal wind variability at 30 hPa, while they differ by a factor of two in their ozone variability.

An alternative measure of the models' representation of the ozone QBO is the vertical distribution of the annual mean equatorial (5°S-5°N) QBO regression coefficient from the MLR analysis (which is represented in terms of ozone mixing ratios for all models and NIWA-3D observations and ozone density for the Randel&Wu ozone). One coefficient is shown in **Figure 8.15a** (the orthogonal one is not shown) for the models in Group B (internal QBO-like oscillation) and in **Figure 8.15b** for models with nudged QBO (Group C). For a better comparison of the QBO signal between the models and observations, the QBO regression coefficient has been multiplied by the typical mean QBO amplitude of 30 m/s. Most of the models in both groups capture well the vertical structure of the QBO signal, but tend to overestimate the magnitude of the response, especially in the lower stratosphere. In the case of ULAQ, this overestimation is particularly evident (more than a factor 2

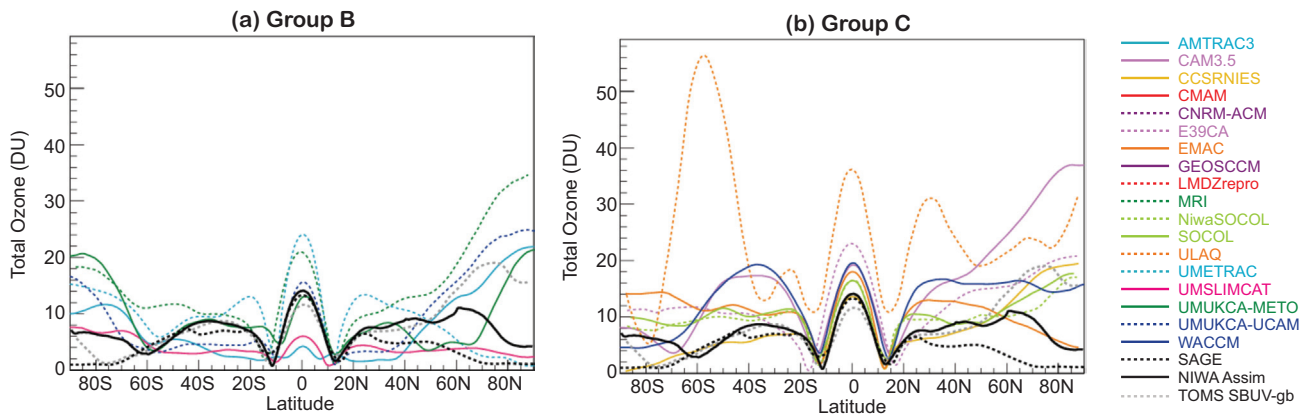


Figure 8.16: Latitudinal distribution of the annual mean QBO amplitude (multiplied by 30 ms⁻¹) in column ozone (DU) from the CCMVal-2 CCMs (1960-2004) and the following observations: TOMS/SBUV+gb (1964-2004), SAGE (1979-2005), and NIWA-column ozone (1979-2007). (a) Group B CCMs. (b) Group C CCMs.

throughout the stratosphere). Among the Group B models, AMTRAC3 and UMSLIMCAT under-estimate the magnitude of the response, and AMTRAC3 also clearly misrepresents the vertical phase of the pattern. The rest of the models in both groups capture the vertical phasing well, and this is particularly true for the nudged QBO models.

8.6.2 QBO signal in column ozone

The latitudinal distribution of the annual mean QBO amplitude from the MLR analysis of column ozone amounts is presented in **Figure 8.16**. All models show a maximum at the equator and minima in the subtropics, in good agreement with observations. Poleward of 20° in both hemispheres, the spread of model results clearly increases. Considering both groups, the equatorial amplitude of the QBO signal in column ozone is within the range of the observations for CCSRNIES, UMUKCA-METO and UMUKCA-UCAM, while it is severely under-estimated

by AMTRAC3 (also featuring a flat latitudinal distribution) and UMSLIMCAT and overestimated by the rest (*i.e.*, the majority) of the models. ULAQ shows the largest QBO amplitude variations, consistent with the overestimation of both variability peaks in **Figure 8.14** (right), but inconsistent with the under-estimation of the wind variability. For the nudged QBO models, problems with the nudging techniques might contribute to the highlighted differences. In general, however, many biases can contribute, such as errors in the QBO-induced residual mean circulation in the lower to mid-stratosphere, the latitudinal extension of the QBO, as well as errors in the vertical gradient of ozone in the vicinity of the induced motions.

Figure 8.17 shows the temporal evolution of the time series reconstruction of the QBO signal from the MLR analysis of column ozone (averaged from 5°S-5°N) for the models and TOMS+gb, Randel&Wu and NIWA-column data. As expected, models that nudge the QBO closely follow the phase of the observed QBO in column ozone,

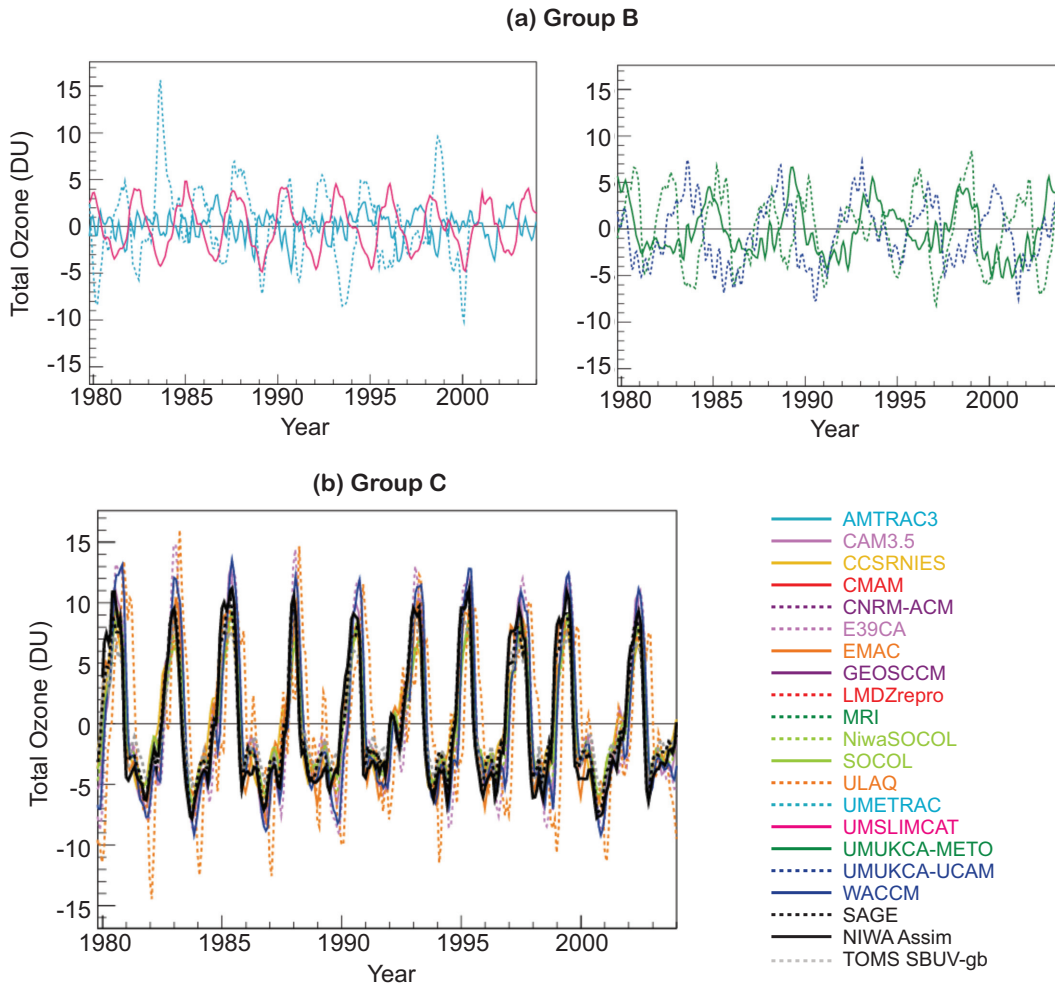


Figure 8.17: Reconstruction of the QBO contribution to the monthly zonal mean column ozone (DU) averaged from 5°S to 5°N. Results from the CCMVal-2 CCMs (in colour; 1960-2004) and the TOMS/SBUV+gb data (1964-2004), SAGE data (1979-2005), and NIWA-column ozone (1979-2006). (a) Group B CCMs. (b) Group C CCMs.

although some of them overestimate the amplitude, consistent with Figure 8.16 and right panels in Figure 8.14. The variability in the Group B models is not expected to be in phase with observations. For the Group B models, Figure 8.17 provides information on the period of the modelled QBO variability in ozone. Among this group, MRI, UMETRAC, UMSLIMCAT show a period close to the observed (~28 months), while UMUKCA-METO and UMUKCA-UCAM overestimate (by almost a factor 2) the typical QBO periodicity. Also note that UMETRAC shows some sporadic large amplitude episodes. AMTRAC3 shows higher frequency (~ 1 year⁻¹) small oscillations and Figure 8.17 therefore confirms that the variability diagnosed in AMTRAC3 is not consistent with the known features of the QBO signal in ozone. From this it can be concluded that the QBO signal in ozone is not represented

in AMTRAC3.

8.7 ENSO Signal in Ozone

The El Niño Southern Oscillation (ENSO) is a tropical atmosphere-ocean phenomenon and a source of large-scale climate variability for the atmosphere-ocean system. Its influence on the stratosphere has been increasingly recognised, with the advent of ensemble modelling and with the availability of longer observational data sets. Most of the published work has focused on the polar lower stratosphere, because of the established teleconnections between the warm phases of ENSO and the mid-latitude North Pacific region (*e.g.*, Hoerling *et al.*, 1997) which can favour the enhancement of mid-latitude planetary waves

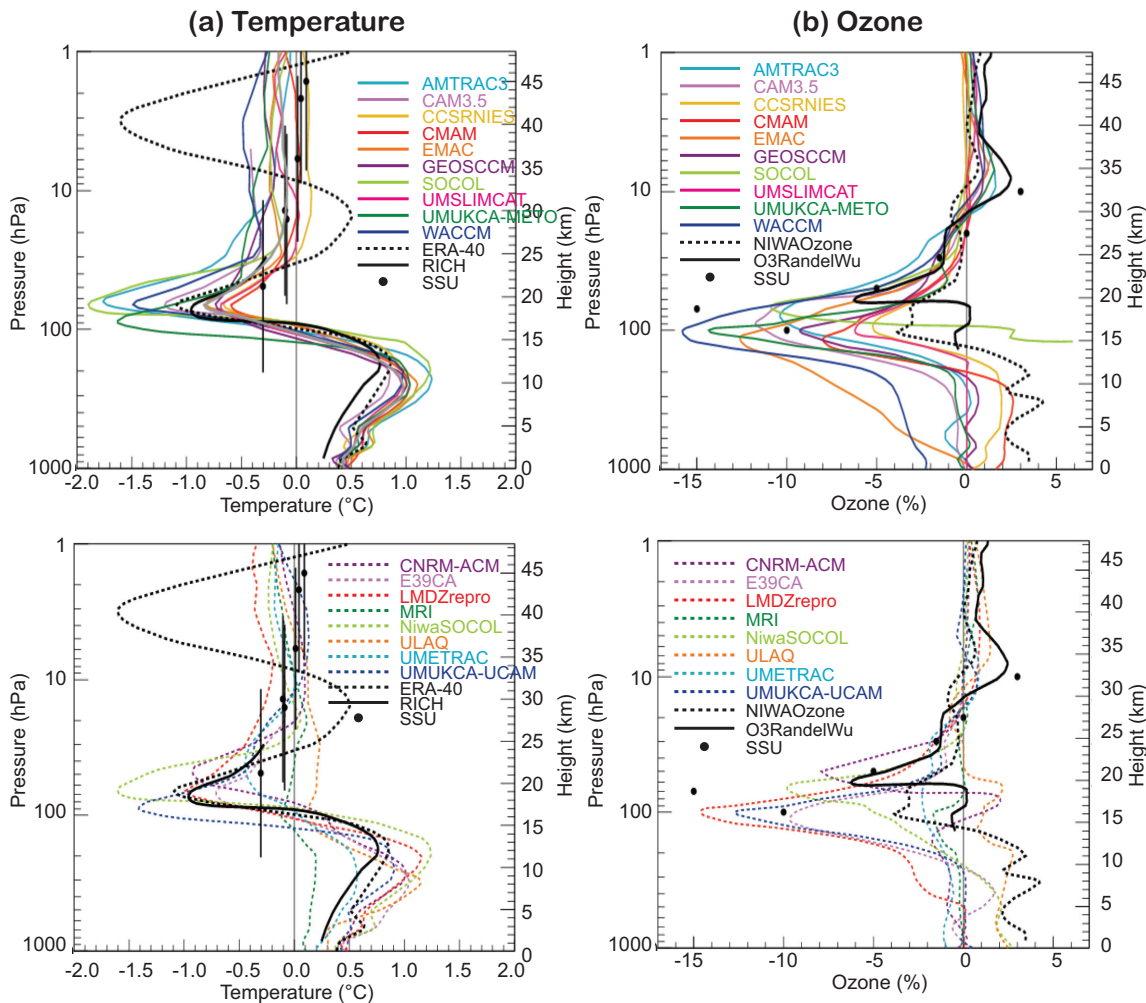


Figure 8.18: Annual mean tropical (25°S-25°N) ENSO regression coefficients from 1000 to 1 hPa for (a) temperature (K) and (b) ozone (%) from the CCMVal-2 CCMs (1960-2004) and observations: RICH radiosonde data (1960-2004), SSU data (1979-2005), and ERA-40 data (1979-2004); NIWA-3D ozone (1979-2004); Randel&Wu ozone (1979-2005). The ENSO coefficients have been multiplied by 2.5 K. In order to better distinguish, the CCMs solid (top) and dashed (bottom) lines have been separated. Black dots represent the Randel&Wu ozone data analysis from Randel *et al.* (2009).

and their upward propagation into the stratosphere. Due to this increase in extra-tropical stratospheric planetary wave activity, warm ENSO events have been found to be associated with anomalous warming and anomalously high geopotential heights in the polar stratosphere, both from observations (van Loon and Labitzke, 1987; Brönnimann *et al.*, 2004; Camp and Tung, 2007; Garfinkel and Hartmann 2007) and comprehensive modelling of the troposphere-stratosphere system (Sassi *et al.*, 2004; Manzini *et al.*, 2006; Garcia-Herrera *et al.*, 2006). These signals in temperature are consistent with signals in ozone during ENSO events (Fischer *et al.*, 2008; Steinbrecht *et al.*, 2006; Brönnimann *et al.*, 2006). The ENSO signal in column ozone for the CCMVal-1 models is discussed in Cagnazzo *et al.* (2009). The polar warming and enhanced ozone associated with warm ENSO events are a manifestation of a stronger Brewer-Dobson circulation during ENSO and a negative signal in both temperature and ozone is therefore also expected in the tropics (Free and Seidel, 2009; Randel *et al.*, 2009; Manzini, 2009).

The ENSO tropical signals in annual mean temperature (left) and ozone (right) from the MLR analysis are shown in **Figure 8.18**. The maximum ENSO temperature and ozone signals occur in the lower stratosphere (~70 hPa), and the patterns are qualitatively similar between models and observations. Most models show a cooling in the lower stratosphere that surrounds the observed cooling of ~1 K, and values from the CCMs vary over approximately a factor of two, with MRI and ULAQ the only outliers. In the upper troposphere, the observed ENSO warming is about 0.6 K and generally lower than that estimated by the models. The node at the tropopause level (where the regression temperature coefficient changes sign) is well reproduced by the models. The modelled ENSO tropical signal in temperature is therefore consistent with Free and Seidel (2009). Between 150 and 50 hPa a reduction in ozone, ranging from -5 to -15%, is found for most models (with MRI and ULAQ again outliers). The comparison with observations shows results from the NIWA-3D and Randel&Wu data sets, and also results from the SAGE I+II data reported in Randel *et al.* (2009). The difference between the latter two results are mainly due to the differences in detail of the respective regression models (the MLR here uses volcanic proxies, while Randel *et al.* (2009) omit volcanic periods). It therefore appears that the ENSO signal is especially sensitive to these differences, because of the overlap of ENSO warm events with the El Chichon (1982) and Pinatubo (1991) volcanic eruptions (Randel *et al.*, 2009). In summary, the model results in Figure 8.18 are broadly consistent with Randel *et al.* (2009), while the ENSO ozone signals derived from the NIWA-3D and Randel&Wu data are somewhat smaller. These differences in the observations serve to highlight the sensitivity to the regression analysis for the ENSO signal and the possibility

that the NIWA-3D and Randel&Wu continuous data time series derived from MRL analysis might not contain all of the observable signals. Note also that ozone variability in the lower tropical stratosphere arises from the combined effects of a number of factors, the QBO, ENSO, the solar cycle and volcanic aerosols: A clear challenge for the MLR analysis approach.

To evaluate the ENSO signal in ozone for the northern polar cap, the methodology developed for the CCMVal-1 models by Cagnazzo *et al.* (2009) has been applied to the CCMVal-2 models. The results are shown in **Figure 8.19**, for the relationship between the February-March averaged north polar cap ENSO response in the temperature and column ozone fields. As in Cagnazzo *et al.* (2009), the ENSO signal has been extracted by calculating difference fields between composites of warm ENSO and NEUTRAL years. Warm ENSO years are defined as the four largest events in the period 1980-1999 and NEUTRAL years are the remaining years when both the four largest warm and cold ENSO events have been excluded. During the period (1980-1999), the cold ENSO events are smaller in magnitudes and have not been found to significantly affect the stratosphere (Manzini *et al.*, 2006).

In agreement with Cagnazzo *et al.* (2009), a clear positive correlation is found between the modelled column ozone and temperature anomalies at high latitude (0.87, significant at more than 99.9%) supporting the idea that anomalies in temperature and column ozone are influenced by the same (Brewer-Dobson circulation) mechanism. This linear relationship is consistent with the one expected from interannual variability: the slope parameter deduced from Figure 8.19 (about 5.5 DU/K) is comparable, within the sampling uncertainty, to the slope calculated using the ERA-40 temperature and NIWA-column ozone from the individual years (Figure 8.8), as well as the one deduced from the CCMVal-1 models, shown in Cagnazzo *et al.* (2009). Therefore, Figure 8.19 also shows that the spread in the CCMVal-2 model responses is due to internal variability. However, for the CCMVal-2 models there is a less distinct dominance of the cases clustered in the upper-right quadrant (where the signature of observations is located), suggesting that a smaller percentage of the models achieve positive temperature anomalies and increased ozone during ENSO, than the CCMVal-1 models discussed by Cagnazzo *et al.* (2009).

Cagnazzo *et al.* (2009) have shown that CCMVal-1 model simulations that did not have a strong enough extra-tropical ENSO teleconnection pattern in the troposphere did not report a temperature and ozone signal in the stratosphere. This result is found also for the CCMVal-2 models, although in the case of CCMVal-2, models with a significant tropospheric ENSO teleconnection also show negative temperature and decreased ozone responses (not shown). The spread of the CCMVal-2 modelled response therefore

appears to be influenced more by internal variability than that of the CCMVal-1 models. Distinguishing the role of internal variability and model biases in the ENSO response is therefore less straightforward for the CCMVal-2 models. The inclusion and/or a more detailed representation of additional forcings that may interfere with the ENSO signal, such as the QBO, the solar cycle and aerosols from volcanic eruptions, could possibly explain the differences between CCMVal-1 and CCMVal-2 simulations. Given the close connections between the CCMs that participated in both projects, the CCMVal-1 and CCMVal-2 results are not actually statistically different.

8.8 Volcanic Aerosols

Volcanic eruptions can have a significant impact on stratospheric ozone. Eruptions of sufficient strength inject SO_2 into the stratosphere, which is then chemically converted to sulphate aerosols. Volcanic induced ozone changes are related to the effect of volcanic sulphate aerosols on the chemical composition and the radiative balance of the lower stratosphere. Volcanic aerosols provide surfaces for heterogeneous reactions to occur, which can alter the partitioning of catalytic ozone destroying families including NO_x and ClO_x . Volcanic aerosols also reflect and scatter incident solar radiation, leading to changes in the photolysis of chemical species, and absorb outgoing longwave radiation, leading to additional heating of the lower stratosphere.

Observed column ozone reduction after the Mt.

Pinatubo and the El Chichón eruptions range from about 2% in the tropics to about 5% (Pinatubo) and 2-3% (El Chichón) in mid-latitudes (Angell, 1997; Solomon *et al.*, 1998). Very large ozone losses were observed after the Mt. Pinatubo eruption at high northern latitudes in February and in March, for example Randel *et al.* (1995) found losses of 10% in total column ozone in 1992 northward of 60°N and 10-12% in 1993. Ozone-sonde profiles after the Mt. Pinatubo eruption show that the concentration did not decrease uniformly at all altitudes (Hofmann *et al.*, 1993; Grant *et al.*, 1994). After the Agung eruption in 1963 a slight increase in global total column ozone was found (Angell, 1997), possibly due to the suppression of nitrogen oxides in the low-chlorine conditions (Tie and Brasseur, 1995).

The methods used to simulate the volcanic impact in the models have been introduced in detail in Chapter 2. Heterogeneous chemical reactions on the volcanic aerosol surfaces are calculated using a prescribed zonal-mean aerosol surface area density (SAD) time series. In the CCMVal-2 model runs, most models have prescribed SADs using the data set compiled and made available through the SPARC Assessment of Stratospheric Aerosol Properties (Thomason and Peter, 2006). The radiative effects of volcanic aerosols have been incorporated into the model in a number of different ways or, in some cases, completely neglected. Chapter 2 (Table 2.18) summarizes the different methods used by the different models, which include (1) no simulation of direct radiative effects, (2) prescribed heating rate anomalies based on offline radiative calculations, (3) online radiative calculations using

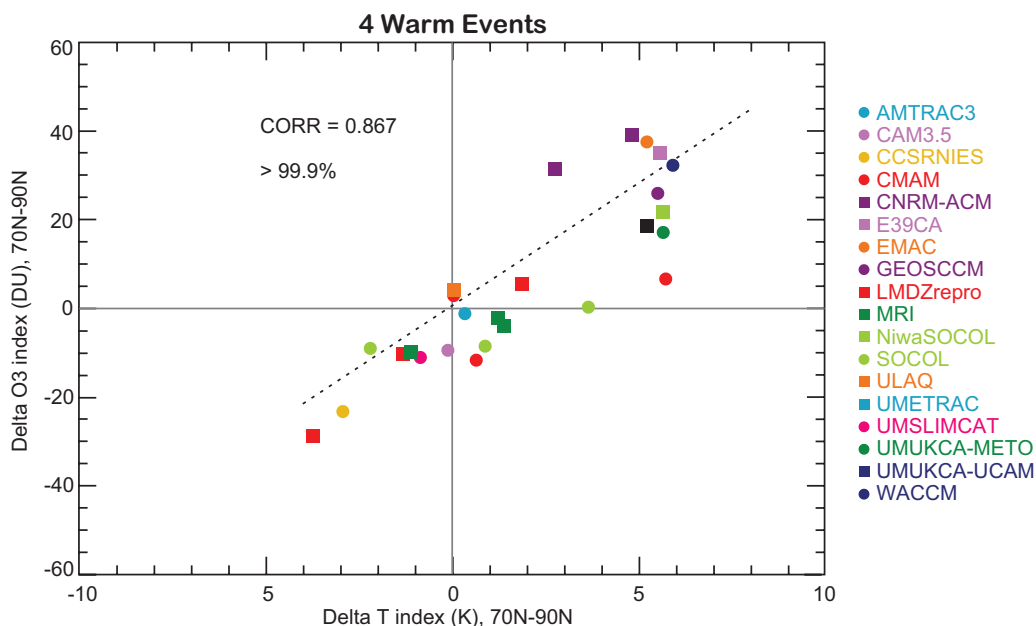


Figure 8.19: Scatter plot of the February-March polar cap ENSO anomaly in column ozone (DU) versus temperature (K, 30-70 hPa average). Black star: NIWA-column ozone versus ERA-40 temperature signature. Colours: CCMVal-2 CCMs. The polar cap averages are computed over 70°N - 90°N .

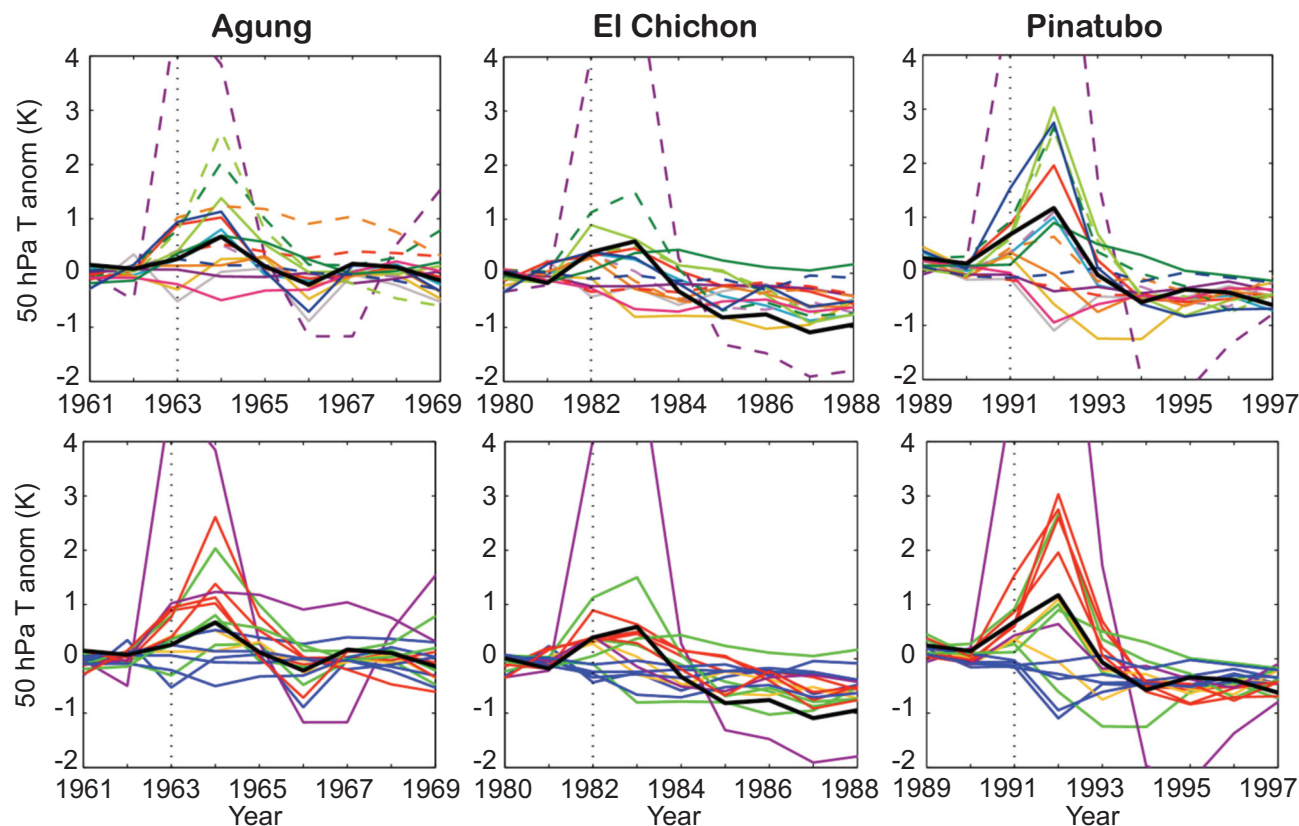


Figure 8.20: Annual mean global mean 50 hPa temperature anomalies from pre-volcanic conditions for the Agung, El Chichón and Pinatubo eruptions. Top: model results colour-coded by model. Bottom: results colour-coded by type of volcanic heating parameterisation used, including: optical properties derived from SADs (red), optical properties from SAGE/GISS data set (green), prescribed heating rate anomalies (yellow), none (blue), full aerosol microphysics (purple). ERA-40 50 hPa temperature anomalies are shown in both plots in black.

aerosol properties estimated from observations, (4) online radiative calculations using optical depths derived from the SPARC SAD data set (also based on observations) and (5) full microphysical modelling of volcanic aerosols based on prescribed stratospheric influx of volcanic SO_2 .

8.8.1 Global mean temperature response

The result of volcanic forcing on stratospheric temperatures can be seen most simply through inspection of global-mean annual-mean temperature time series. These are shown at 50 hPa in **Figure 8.20** (top panel), as anomalies from pre-volcanic conditions for the three eruptions of the 1960–2000 time period: Agung (1963), El Chichón (1982) and Mt. Pinatubo (1991). The anomalies are calculated as deviations from the mean of the 5 years (3 years for Agung) preceding the year of the eruption. There is a considerable spread in the post-volcanic eruption temperatures in the models. For example, in 1992 after the Pinatubo eruption, the changes in 50 hPa temperature range from +9 to -1 K, while the observations show a +1 K change. CNRM-ACM appears as an outlier in this diagnostic, with

temperature increases much larger than the other models or the observations. This is related to how the radiative scheme responds to the volcanic aerosols. Subsequent runs of the CNRM-ACM model, in which the aerosol properties have been modified to exhibit less absorption, have shown temperature evolution in the range of that of the CCMVal-2 CCMs (Martine Michou, personal communication, 2009). The temperature response in all of the models is strongly dependent on the parameterisation method employed to simulate the direct radiative effects of volcanic aerosol loading. In the lower panel of **Figure 8.20** the anomalies have been replotted, but colour-coded by parameterisation method. This plot shows that using aerosol optical depths derived from the SPARC SADs (red: NiwaSOCOL, SOCOL, WACCM, CMAM) leads, at least in the Pinatubo and Agung eruptions, to anomalously large temperature perturbations compared to those estimated from the ERA-40 data set. Those models that did not include radiative effects of volcanic aerosols (blue: CAM3.5, GEOSCCM, LMDZrepro, UMSLIMCAT, UMUKCA-UCAM) show little change in 50 hPa temperature, although two models show modest (~ 1 K) decreases after the Pinatubo eruption,

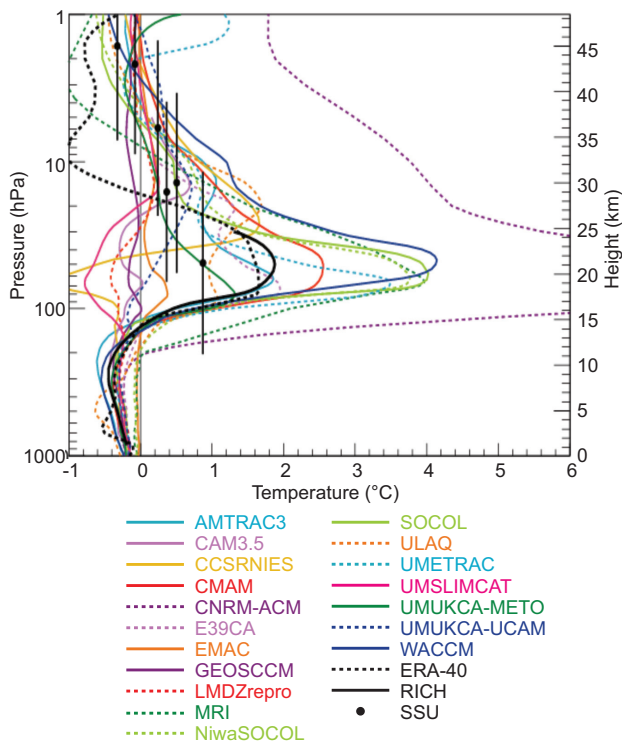


Figure 8.21: Annual mean tropical (25°S-25°N) contribution from the volcanic basis function from CC-MVal-2 CCMs (1960-2004) and observations (ERA-40, SSU and RICH) to temperature in Kelvin (K) for Pinatubo (averaged over 24 months after the eruption) from 1000 to 1 hPa.

as might be expected due to chemical induced ozone decreases. Finally, the models which employ optical depth estimates from GISS (green: AMTRAC3, CCSRNIES, MRI, UMUKCA-METO) and those which use prescribed heating rates (yellow: E39CA, EMAC) show (for some models, *i.e.*, AMTRAC3, E39CA, and UMUKCA-METO) quite good agreement with the observations. However, there are also some outliers: *e.g.*, the CCSRNIES model

shows cooling after the El Chichón and Pinatubo eruptions even though aerosol radiative heating is included.

8.8.2 Vertical temperature response

Inspection of the vertical structure of the temperature anomalies can help evaluate the reason for the discrepancies between models. **Figure 8.21** shows the annual mean tropical contribution from the volcanic basis function for Pinatubo (responses for Agung and El Chichón are shown in Figure S8.10) averaged over 24 months after the eruption for temperature in the tropics, where the temperature increases are largest. The structure of the anomalies is generally consistent between the models, with maximum heating at ~50 hPa (20 km), in good agreement with observations. There is excellent agreement between the models that show the largest response in the region of maximum heating in Figure 8.21 and those that show the largest temperature response in Figure 8.20. The models which include no direct aerosol heating show a negative sign in their temperature response. A number of outliers in Figure 8.20 also show deviations from the general vertical structure. For example, CCSRNIES, which showed post-volcanic cooling at 50 hPa shows a positive response in Figure 8.21 only at heights above 40 hPa, and negative ones between 50 and 100 hPa. On the other hand, the EMAC response is small and restricted to heights below 50 hPa, which helps explain why the EMAC anomalies of Figure 8.20 are different from the other models using prescribed heating rates. The latitude-height structure of the Pinatubo temperature response is shown in Figures S8.11 and S8.12.

8.8.3 Ozone response

Figure 8.22 shows global-mean, annual-mean total-column ozone anomalies compared with pre-volcanic conditions. Local minima in the years after the El Chichón and Pinatubo eruptions are associated with the effects of the

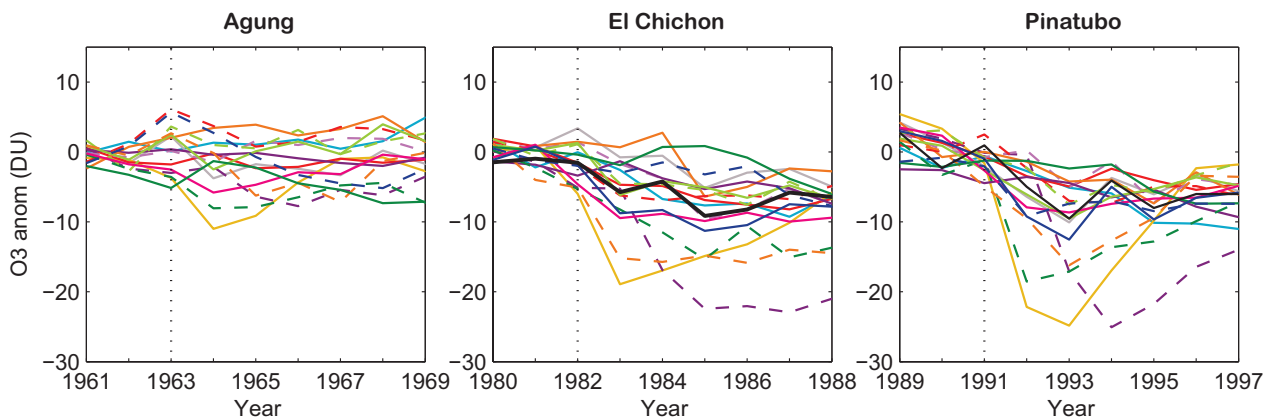


Figure 8.22: Annual mean global mean column ozone anomalies from pre-volcanic conditions for the Agung, El Chichón and Pinatubo eruptions. Ozone anomalies from the TOMS+gb data set are shown in black.

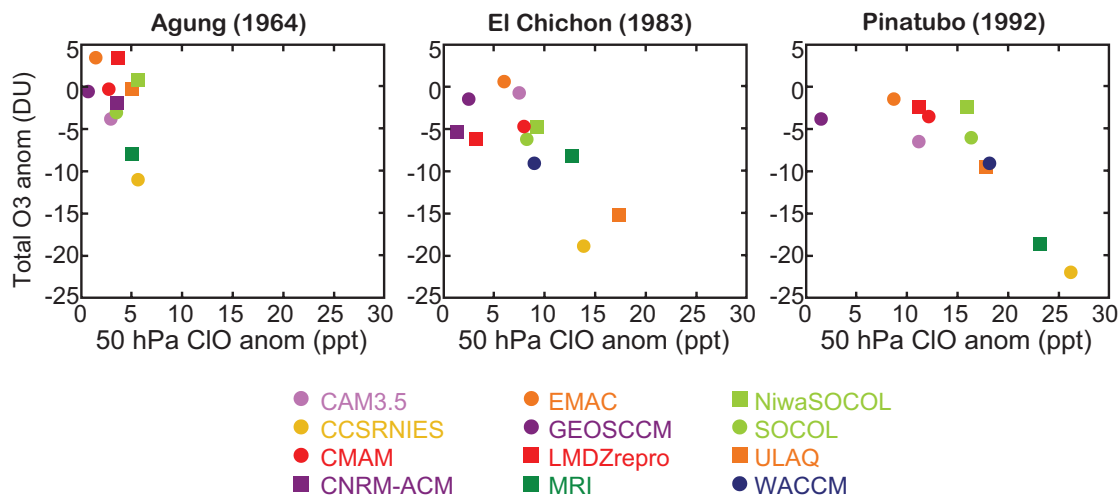


Figure 8.23: Post volcanic eruption annual mean global mean anomalies of column ozone as a function of similarly calculated anomalies in ClO at 50 hPa, for the models that have reported ClO mixing ratios.

volcanic aerosols. Note that in these plots the anomalies are the result of a number of factors including volcanic effects, but also the EESC related trend and the QBO. The observed anomalies after the El Chichón and Pinatubo eruptions were of the order of 10 DU. There is a large degree of scatter in the model results, ranging from some models showing post-volcanic decreases of up to 15–20 DU (CCSRNIES, MRI, ULAQ) and, for El Chichón, small post-eruption increases (EMAC, UMUKCA-METO). For the Agung eruption, some models show a slight increase in the year of the eruption, however, it is impossible to attribute any ozone changes to the volcanic effects, as the spread in modelled values stays relatively constant over the time span shown. Slight differences in the vertical structure of the ozone response (Figure S8.13) can help shed light on why the global-mean total ozone time series in Figure 8.22 differ. The models generally show the largest ozone loss at 30 hPa (25 km). After Pinatubo, two models (CCSRNIES and ULAQ) show responses at lower heights than the other models and these two models are among the models with the largest total ozone losses. The latitudinal distribution of total ozone losses is shown in the supplementary material (Figure S8.14).

Since a large amount of volcano-related ozone loss is related to heterogeneous chemistry, one would expect the models with largest ozone loss to have the largest amounts of chlorine activation. **Figure 8.23** confirms this, showing the ozone anomaly in the year following each eruption as a function of the anomaly in ClO at 50 hPa. For each eruption, there is a relatively linear relationship between ozone loss and chlorine activation. Note that by choosing to look only at the year after each eruption, the relationship between ClO and ozone for CNRM-ACM is not well represented by these plots, since this model displays maximum ClO and ozone anomalies three years after each eruption,

and in fact shows negative ClO anomalies for the first year after the Mt. Pinatubo eruption (with large increases afterwards). Latitude-time plots of ClO (not shown) and total ozone abundances (Figure S8.14) confirm that the models with largest total ozone loss, including CCSRNIES and ULAQ, are characterized by chlorine activation and ozone loss extending from the tropics to the high latitudes. Thus, the cause of the anomalous ozone loss in these models is the anomalous chlorine activation, which may itself be related to biases in total chlorine since both models received low grades representing Cl_y in the middle stratosphere (Chapter 6) or too low stratospheric temperatures (Chapter 4).

An interesting feature of the observed ozone loss after the Mt. Pinatubo eruption is the hemispheric asymmetry: NH ozone levels (especially in mid-latitudes) have been observed to decrease after the eruption, while levels in the SH were relatively unperturbed (WMO, 2007). None of the CCMVal-2 models reproduce the observed hemispheric asymmetry in post-Pinatubo ozone loss, for either full hemispheric means or for mid latitudes (see Figures S8.15 and S8.16). Most models have post-Pinatubo SH ozone loss which is comparable to or greater than that observed, while NH ozone loss is less than that observed. Whether or not the models have a QBO (internally generated or nudged) does not appear to have an appreciable effect on this result.

8.9 Conclusions

Although the MLR analysis is a powerful tool for synthesizing the relative influence of the variability sources on natural ozone variation, it cannot take into account the fact that the net effect of the natural variations on ozone is usually a non-linear combination of the single contributions of variability factors. Non-linearities have been reported for

the combined ENSO and QBO signal (Calvo *et al.*, 2009), the solar-QBO and volcanic signals (Lee and Smith, 2003), solar-QBO signals (Smith and Matthes, 2008; Camp and Tung, 2008; Matthes *et al.*, 2010), the solar-SST signal (Marsh and Garcia, 2007; Austin *et al.*, 2008), and ENSO, QBO, and solar interconnections (*e.g.*, Kryjov and Park, 2007; Kuroda, 2007; Kodera *et al.*, 2007). Many of these inter-connections of the natural variability sources are objectives of current research.

Another limitation of the assessment in this chapter is the relatively short observational record which limits the statistical significance of many of the responses to individual components. This is especially true for the 11-year solar cycle, where only data for two and a half cycles are available, and for ENSO, a relatively sporadic event, usually occurring with a wide variety of amplitudes. Additionally, large volcanic eruptions coincided with solar maximum phases of the solar cycle. Another limitation of the available ozone observational time series is that they are reconstruction by statistical models (usually MLR analysis) in order to provide a continuous time series without missing data. Therefore, there is the possibility that the MLR analysis of the reconstructed time series might return signals affected by the periods with missing data.

Because of these limitations, it is still very difficult to quantitatively evaluate (grade) the model performance by individual natural variability factor, especially for the solar cycle, ENSO and volcanoes, and relate their relative importance to the evolution and prediction of stratospheric ozone. Note that Dameris *et al.* (2006) show a delay of

ozone recovery due to solar cycle effects.

Given that estimates of the annual cycle in ozone are the most reliable, the quantitative evaluation of the model performance is carried out only for the climatology and interannual variability of the annual cycle in ozone (Figure 8.24, Table 8.5). The performance of the QBO signal in ozone could be a second candidate for a quantitative evaluation. However, the modelling of this phenomenon in CCMs is in a too primitive stage to apply performance metrics.

For the case of the ozone annual cycle climatology and interannual variability, the model performance is quantified following Taylor (2001). The respective correlations and normalised standard deviations discussed in Sections 8.3 and 8.4 are combined in one grade by means of Equation 5 of Taylor (2001). The results are summarized in matrix form in Figure 8.24. Thereafter, the information in Figure 8.24 is used in the following summaries, by variability factor and model-by-model.

8.9.1 Summary by process

Summary on annual cycle

The comparison with MLS data shows that the processes leading to the annual cycle in the upper stratosphere are well captured by the models: the anti-correlations between temperature and ozone at 1 hPa are broadly captured and provide a simple check of photolysis scheme (Section

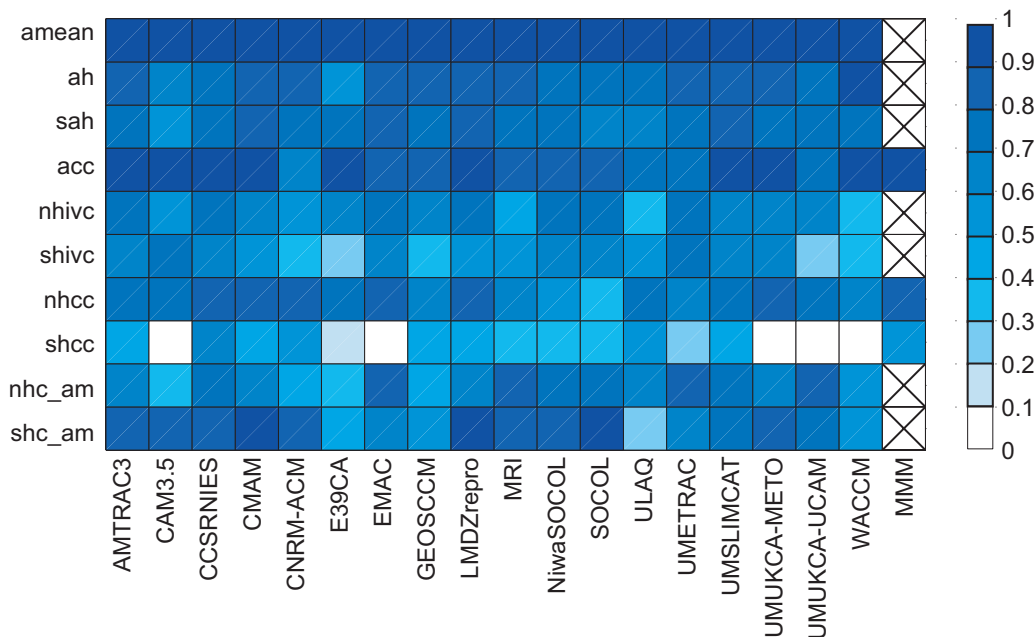


Figure 8.24: Matrix displaying the model performance (see colour bar), following Equation 5 of Taylor (2001), for the normalised Taylor diagrams discussed in the chapter. See Table 8.5 for definitions of the assessment factors.

Table 8.5: List of metrics used in Chapter 8.

Metric	Description	Details
amean	Annual zonal-mean ozone	500-1 hPa, 90°S-90°N
ah	Annual harmonic in ozone from the MLR analysis	500-1 hPa, 90°S-90°N
sah	Semiannual harmonic in ozone from the MLR analysis	500-1 hPa, 90°S-90°N
acc	Annual cycle of near global column ozone	60°S-60°N, January to December climatology
nhvc	Monthly standard deviation of column ozone	60°N-90°N, January to December
shvc	Monthly standard deviation of column ozone	60°S-90°S, January to December
nhcc	Column ozone climatology	60°N-90°N, January to December
shcc	Column ozone climatology	60°S-90°S, January to December
nhc_am	Northern annular mode - ozone relationship	60°N-90°N, March
shc_am	Southern annular mode - ozone relationship	60°S-90°S, November

8.3). The magnitude of the annual cycle and the transition to summer conditions are also well reproduced by the models. However, in the lower stratosphere a few models (UMUKCA-METO and UMUKCA-UCAM) do not reproduce the anthropogenic deviation of the annual cycle (polar ozone depletion) that dominates the late winter and spring in the SH.

In comparison with HALOE, the CCMVal-2 models show a larger spread in their response to the annual cycle, in the NH and SH spring, upper troposphere and lower stratosphere, than the CCMVal-1 models. This may simply be due to the fact that more CCMs participated in this evaluation. CCMVal-2 model outliers are CCSRNIES, which shows unusually large ozone values at 10 hPa in March at the equator and in October at 80°S, and CNRM-ACM at 50 hPa which shows unusually small values at all except polar latitudes.

The assessment of the performance of the models for the annual cycle in ozone that is summarized in Figure 8.24 (ah and sah diagnostics), implies that the vertical and latitudinal distribution of the annual cycle in stratospheric zonal monthly mean ozone is very well represented by the majority of the models. There are only two outliers, CAM3.5

and E39CA, respectively showing poor performance in the semi-annual and annual harmonic ozone diagnostics, possibly because of their low top. Concerning the annual mean (amean diagnostic) and the annual cycle in near global column ozone (acc diagnostic), all models perform very well. However, this result does not translate in to a lack of global mean ozone bias, as reported in Table 8.2. Major outliers in global mean bias are E39CA and UMUKCA-UCAM, which both overestimate the near-global ozone as well as the North and South polar ozone.

Summary on interannual polar variability

The observed annual cycle in polar column ozone variability is well reproduced by all models, in the sense that all show a minimum in variability in the summer seasons (Section 8.4). In the NH dynamically active period, most of the models under-estimate the interannual polar variability, indicating a common bias. With the exception of CAM3.5, Figure 8.24 (nhvc and shvc diagnostics) shows that models (CNRM-ACM, MRI, ULAQ and WACCM) with poor performance in interannual variability in the NH also perform poorly in the SH, suggesting basic problems in the dynamical core of the models, possibly related to resolution and the parameterisation of the effects of unresolved gravity waves. The model performance in the annual cycle in polar ozone climatology (nhcc and shcc) shows instead a marked hemispheric asymmetry, with good to very good performance in the North polar cap, but poor to very poor in the Southern polar cap. The latter case is therefore highlighted as a systematic bias, due to persistent problems in the combined representation of the chemical and dynamical processes characterizing the morphology of the ozone hole.

The majority of models reproduce quite well the relationship between winter mean heat flux and spring-to-fall ozone ratio in both the NH and SH. This result suggests that the sensitivity of ozone to the heat fluxes is realistic. The only outlier is the ULAQ model, which appears to severely under-estimate the relationship in the NH. The models reproduce the observed ozone-temperature relationship quite well; although in the NH the ozone is less responsive to temperature perturbations in a number of the models than in the observations. Among the models with low sensitivity is again ULAQ, while the relationship is substantially overestimated by CNRM-ACM. In the SH, the spread of the models surrounds the observations, as in the case of the ozone standard deviation. When the parameters of heat flux versus ozone and heat flux versus temperature fits are compared (not shown) there is a good correlation (>0.6) between them in both hemispheres. This indicates that models with enhanced polar temperature sensitivity to planetary wave activity also exhibit an enhanced sensitivity of polar ozone to planetary wave activity.

The regression of the column ozone on to the simplified AM index further confirms that the modelled interannual polar ozone variations are due to the known dynamical processes affecting the variability of the stratospheric vortex and that these processes and their connection to ozone are generally well simulated for the majority of the models. Figure 8.24 shows that models previously highlighted with poor performance in interannual variability, are those that tend to perform poorly also in the ozone variations associated with the annular mode (nhc_am and shc_am).

Summary on 11-year solar cycle

Most models imposed a solar cycle in the CCMVal-2 REF-B1 simulations (sc group), with only five that did not (no-sc group, *i.e.*, GEOSCCM, ULAQ, UMUKCA-METO, UMUKCA-UCAM, UMETRAC, Section 8.5). The solar cycle in total column ozone is qualitatively well represented in the sc group, although with some amplitude spread. Most models reproduce 70–80% of the observed solar total column ozone variations from 60°S to 60°N. MRI, UMSLIMCAT and WACCM show best agreement with observations, while CNRM-ACM, CCSRNIES, CAM3.5, and ULAQ show the worst agreement. The vertical structure of the tropical solar signal in ozone and temperature is more difficult to model. While the direct solar response in temperature and ozone in the upper stratosphere is well represented (best for WACCM, CMAM, AMTRAC3, and UMSLIMCAT, worst for LMDZrepro) the vertical structure in the tropics below 10 hPa varies a lot among the models but also among different observational data sets. Especially in the lower stratosphere uncertainties are large and might be related to non-linear interactions with a number of signals (solar, QBO, ENSO, volcanos) that might not be handled correctly in a MLR as discussed earlier. Another limiting factor might be the fact that we only used one simulation from each model. An ensemble mean for the models that delivered several simulations might reduce the large uncertainties in the middle and lower stratosphere as shown by Austin *et al.* (2008). In general the agreement between the models and between the models and observations is better for ozone than for temperature. The latitudinal representation of the solar response in total column ozone shows improved representation compared with CCMVal-1 but a large spread especially at mid- to high latitudes due to large interannual variability.

Compared to CCMVal-1, the way in which the solar cycle in radiation and chemistry is represented has been improved, by prescribing daily varying spectrally resolved irradiance data from the SOLARIS project (Matthes *et al.*, 2007) instead of scaling to the F10.7 cm solar radio flux as used in CCMVal-1. Nevertheless, the modelled responses still show large differences that might be related to differences in the performance of the radiation schemes (com-

pare Chapter 3, Section 3.6), the photolysis schemes (compare Chapter 6) or to dynamical and transport differences that are very difficult to separate.

Summary on QBO

Metrics are not computed for the QBO signal in ozone because the status of the modelling of the QBO in CCMs is still at a primitive stage (Section 8.6). Some AGCMs in recent years have been able to simulate a quite realistic QBO in zonal winds and related dynamical quantities, but it does not seem that this expertise has passed to the CCMs, possibly because of the computational and/or developmental constraint of the additional chemical modelling. The QBO modelling in the CCMs as implemented for CCMVal-2 therefore remains an outstanding problem.

In summary, there are three groups of models: Group A with negligible tropical variability, Group B with intermediate to large tropical variability, and the Group C models, with externally imposed tropical variability (Table 8.4). The QBO signal in ozone is not simulated by any of the Group A models nor by the AMTRAC3 model of Group B. Although AMTRAC3 showed some signal in tropical variability, it fails in all diagnostics. The rest of the models in Group B, namely MRI, UMETRAC, UMSLIMCAT, and UMUKCA-METO, and UMUKCA-UCAM, and all models of Group C, show a QBO signal in ozone, *albeit* with some biases. From the MLR analysis, it is found that these models show a comparable spread in the amplitude of the QBO signal in ozone. Among the models with nudged QBO variability, large overestimations of the amplitude of ozone variations are found for ULAQ, indicating a problem with the nudging specification. Among the models with internal QBO variability, MRI, UMETRAC, UMSLIMCAT show a periodicity close to the observed average, while UMUKCA-METO and UMUKCA-UCAM overestimate (by almost a factor 2) the typical QBO periodicity.

Summary on ENSO

For most models, the tropical ENSO signal in temperature is consistent with that estimated by available observations in the lower stratosphere and upper troposphere, in the sense that the model results envelop the observed signatures (Section 8.7). Most models show a comparable response in ozone, although with a spread. In this case, it is hard to judge if the modelled ozone variations are consistent with the observations, because of the large uncertainty in the observational data used. By looking at column ozone a clear picture emerges, with the spread of the model responses explained by interannual variability. Note indeed that the slope (from the ensemble of models) deduced by Figure 8.19 is consistent with the slope estimated by observations in Figure 8.8.

It is concluded that an ENSO signal in temperature and ozone is emerging from the models, especially in the tropical lower stratosphere, where most of the models show a cooling and an ozone reduction. However, because of the large role of interannual variability and the uncertainty in the observations, it is not possible to measure the model performance in the simulation of the ENSO signal in ozone.

Summary on volcanic aerosols

The models show a considerable spread in their simulated response to volcanic eruptions (Section 8.8), as seen in modelled temperature and ozone responses. The fact that many fundamentally different methods have been employed to parameterise the direct effect of volcanic aerosols on the radiative transfer of the stratosphere (Figure 8.21) helps explain, at least in part, the wide range of post-eruption temperature anomalies seen in the different models. For example, models that estimate aerosol optical depth from the SAD data set of WMO (2007) consistently overestimate lower stratospheric temperatures after the Mt. Pinatubo eruption compared to the ERA-40 data set. On the other hand, models which use the GISS aerosol optical depth data set lead to wide ranging estimates of lower stratospheric heating. Post-eruption changes in total column ozone are well correlated with changes in lower stratospheric CIO. It thus appears that while most models use a common aerosol SAD data set to drive anomalous post-eruption chemistry, the models display differing degrees of sensitivity to those aerosols, leading to differing amounts of chlorine activation and associated ozone loss. None of the CCMVal-2 models reproduce the observed hemispheric asymmetry in post-Pinatubo ozone loss, for either full hemispheric means or for mid-latitudes.

8.9.2 Model by model summary

A model by model summary is provided that is based on the grading of the metrics listed in Table 8.5 as well as some approximate grading for the remaining variability factors considered. In a few cases, the evaluation of the modelled key processes responsible for natural ozone variations has not been possible, because the respective external forcing was not included in the models. Three broad groups are identified: (1) models that simulate natural ozone variations well with better or mean performance in most diagnostics, (2) models that simulate natural ozone variations and with mixed and/or limited success, and (3) models that are outliers in many diagnostics for natural ozone variations.

AMTRAC3 accurately represents the annual mean and the annual cycle in ozone, in near global and northern polar col-

umn ozone. The variability of column ozone in both polar caps is well represented, while the annual cycle in southern polar cap column ozone is poor. It has a good representation of the solar cycle in ozone and temperature. This model fails to reproduce the QBO signal in ozone. The tropical ENSO signal in temperature and ozone is within the cluster of model responses. The model compares quite well with the observed volcanic effects (optical properties from SAGE/GISS are used for the volcanic aerosols). Overall, AMTRAC3 simulates natural ozone variations well, with better or mean performance in most diagnostics.

CAM3.5 performs well to very well for the annual mean and the annual cycle in ozone, in near global and North polar column ozone, but it shows a poorer performance in the ozone semi-annual harmonic and in the column ozone variability for both polar caps than other models. It does not accurately represent solar cycle effects in temperature and ozone. The amplitude of the ozone response to the nudged QBO is moderately overestimated. The tropical ENSO signal in temperature and ozone is within the cluster of model responses. This model does not use a parameterisation of volcanic effects and therefore it does not show a volcanic response. CAM3.5 is an outlier in many diagnostics for natural ozone variability possibly related to its low top.

CCSRNIES performs very well for the annual mean and the annual cycle in ozone, in near global and northern polar column ozone. The annual cycle in southern polar cap column ozone and the variability in both polar caps are well represented. It shows unusually large ozone peak values at 10 hPa that might be related to its fast tropical ascent (Chapter 5), and/or its poor performance for nearly all photolysis rates (Chapter 6). This model uses spectrally resolved data to represent the solar cycle and consistently shows large shortwave heating rates. However the solar response in temperature is biased low compared to most models and large biases occur in the solar ozone and temperature signal in the tropical lower stratosphere which lead to large biases in the solar response of total column ozone. The ozone response to the nudged QBO is excellent. The tropical ENSO signal in temperature and ozone is within the cluster of model responses. The model uses SAGE/GISS data to model the effect of volcanoes but fails to reproduce the observed volcanic signals in temperature and ozone. Overall, CCSRNIES simulates natural ozone variations with mixed and/or limited performance in most diagnostics.

CMAM accurately represents the annual mean and the annual cycle in ozone, in near global and northern polar column ozone. The variability of column ozone in both polar caps is well represented, while the annual cycle in southern polar cap column ozone is poor. It uses spectrally

resolved data to represent the solar cycle and is among the best performing models for the solar cycle in the upper stratosphere, but shows larger discrepancies in the middle and lower stratosphere in the tropical ozone signal. This model does not have a QBO signal in ozone. The tropical ENSO signal in temperature and ozone is within the cluster of model responses. This model uses optical properties from SADs to represent volcanic aerosols and tends to overestimate its effects. Overall, CMAM simulates natural ozone variations well, with better or mean performance in most diagnostics.

CNRM-ACM performs well to very well for the annual mean and the annual cycle in ozone, in near global and polar column ozone, while the variability of column ozone in both polar caps is poor. The 50 hPa ozone concentrations in NH spring and autumn are biased low. The solar signal in temperature and ozone is substantially overestimated and is the largest among all models. This model does not have a QBO signal in ozone. The tropical ENSO signal in temperature and ozone is within the cluster of model responses. This model includes full volcanic aerosol microphysics, but due to the way the radiative scheme responds to volcanic aerosols, it produces anomalously large temperature responses to volcanic effects. CNRM-ACM is an outlier in many of the diagnostics for natural ozone variability shown in this chapter.

E39CA performs well to very well for the annual mean and the annual cycle in ozone, in near global and northern polar column ozone. The variability of column ozone in the polar caps is well represented in the north but very poor in the south. The model shows a poorer performance in the ozone annual harmonic and it fails to reproduce the annual cycle in southern polar cap column ozone. It also shows poorer performance in the ozone variations associated with the annular mode, suggesting that the good performance in NH ozone variability might be the results of compensating errors. The global mean column ozone is biased high everywhere. Similarly to CAM3.5, it does not capture the solar temperature signal, possibly due to its low lid. The amplitude of the ozone response to the nudged QBO is slightly overestimated. The tropical ENSO signal in temperature and ozone is within the cluster of model responses. To mimic the effects of volcanic aerosols, prescribed heating rate anomalies are used that provide temperature reactions close to the observed ones. Overall, E39CA simulates natural ozone variations with mixed and only limited success, possibly related to its low lid.

EMAC accurately represents the annual mean and the annual cycle in ozone, in near global and northern polar column ozone. The variability of column ozone in both polar caps is well represented. The model fails to reproduce the

annual cycle in southern polar cap column ozone. It has a good representation of solar induced ozone changes and their effect on heating but shows smaller temperature and ozone responses than most models which result in a lower than observed solar regression coefficient for total column ozone. The amplitude of the ozone response to the nudged QBO is less overestimated than for the rest of the models with nudged QBO, possibly because of the biased low variability in the lower stratosphere. The tropical ENSO signal in temperature and ozone is within the cluster of model responses. EMAC uses prescribed heating rates to simulate the effect of volcanoes but fails to represent it correctly. Overall, EMAC simulates natural ozone variations well, with better or mean performance in most diagnostics.

GEOSCCM accurately represents the annual mean and the annual cycle in ozone, in near global and northern polar column ozone, but shows a poor performance in the annual cycle in southern polar cap column ozone. The variability of column ozone in the polar caps is well represented in the north but very poor in the south. It also shows poor performance in the ozone variations associated with the annular mode. This suggests that the good performance in NH ozone variability might be the result of compensating errors. The global mean column ozone is biased high, in both polar caps. It does not prescribe a solar cycle in irradiance, has no QBO signal in ozone, and did not include radiative effects of volcanic aerosols, and hence does not show a volcanic signal in temperature or ozone. The tropical ENSO signal in temperature and ozone is within the cluster of model responses. Overall, GEOSCCM simulates natural ozone variations with limited success.

LMDZrepro accurately represents the annual mean and the annual cycle in ozone, in near global and northern polar column ozone. The variability of column ozone in the polar caps is well represented in the north but poor in the south. The annual cycle in southern polar cap column ozone is poor. It prescribes solar cycle variations as total solar irradiance (TSI) changes in the heating and spectrally resolved in the photolysis leading to a small short wave heating and therefore largely under-estimates temperature changes when compared to the majority of the models. Solar induced ozone variations are well reproduced. This model does not have a QBO signal in ozone. The tropical ENSO signal in temperature and ozone is within the cluster of model responses. It does not include any volcanic forcing; hence it does not show a response. Overall, LMDZrepro simulates natural ozone variations moderately well, with mean or limited performance in most diagnostics.

MRI accurately represents the annual mean and the annual cycle in ozone, in near global and northern polar column ozone, while the variability of column ozone in both polar

caps is poor. The model fails to reproduce the annual cycle in southern polar cap column ozone. It prescribes spectrally resolved solar irradiance variations leading to the highest shortwave heating rates and relatively large solar cycle temperature and ozone responses as compared with other models, especially in the upper stratosphere. Both the amplitude and the period of the QBO signal in ozone are well represented. However, this model is one of the few that under-estimates the tropical ENSO signal in temperature and ozone. It uses optical properties from SAGE/GISS and overestimates the volcanic effect on temperatures by a factor of almost two. Overall, MRI simulates natural ozone variations with mixed and limited success.

NiwaSOCOL performs well to very well for the annual mean and the annual cycle in ozone, in near global column ozone, and in the variability of column ozone in the northern polar cap. The annual cycle in northern polar cap column ozone is poor and the model fails in the southern polar cap column ozone and variability. The solar response in temperature and ozone is less than in most other models. The amplitude of the ozone response to the nudged QBO is well represented. The tropical ENSO signal in temperature and ozone is within the cluster of model responses. To represent volcanic effects, the model uses optical properties derived from SADs and, except for El Chichón, the volcanic signals are largely overestimated. Overall, NiwaSOCOL simulates ozone variations with mixed and limited success.

SOCOL performs well to very well for well for the annual mean and the annual cycle in ozone, in near global column ozone, and in the variability of column ozone in the Northern polar cap. The model fails to represent the annual cycle in polar column ozone and variability. Compared to NiwaSOCOL it shows a slightly larger solar response in temperature and ozone and very similar QBO and volcanic signals. The tropical ENSO signal in temperature and ozone is within the cluster of model responses. Overall, SOCOL simulates natural ozone variations with mixed and limited success.

ULAQ performs well to very well for the annual mean and the annual cycle in ozone and in near global and northern polar ozone, but it shows a poorer performance in southern polar ozone. The model fails to reproduce the variability of column ozone in both polar caps. It does not prescribe a solar cycle, and the amplitude of the ozone response to the nudged QBO is substantially overestimated. This model under-estimates the tropical ENSO signal in temperature and ozone. The model uses full aerosol microphysics to represent volcanic effects. Except for Agung, the correspondence with observations is remarkable. Overall, ULAQ is an outlier in many of the diagnostics for natural ozone variability shown in this chapter.

UMETRAC performs well to very well for the annual mean and the annual cycle in ozone, in near global and northern polar column ozone, but fails to reproduce the annual cycle in southern polar column ozone. The variability of column ozone in both polar caps is well represented. The global mean in northern polar column ozone is biased low. It does not prescribe solar cycle changes. The period of the internally generated QBO signal in ozone is well represented, while the amplitude is biased high. The tropical ENSO signal in temperature and ozone is within the cluster of model responses. It was not evaluated in the volcanic section since data were delivered too late. Overall, UMETRAC simulates natural ozone variations with mixed and/or limited success.

UMSLIMCAT accurately represents the annual mean and the annual cycle in ozone, in near global column ozone. The variability of column ozone in both polar caps and the annual cycle in northern polar column ozone are well represented, but the model fails to reproduce the annual cycle in southern polar column ozone. It includes spectrally resolved data and shows larger than average solar temperature and ozone signals, leading to a good correspondence in the total column ozone solar regression coefficient. The period of the internally generated QBO signal in ozone is well represented, while the amplitude is biased low. The tropical ENSO signal in temperature and ozone is within the cluster of model responses. It does not include radiative effects of volcanic aerosols and shows modest decreases after the Pinatubo eruption, as expected from chemical induced ozone decrease. Overall, UMSLIMCAT simulates natural ozone variations well, with better or mean performance in most diagnostics.

UMUKCA-METO accurately represents the annual mean and the annual cycle in ozone, in near global and northern polar column ozone. The variability of column ozone in both polar caps is well represented. The model fails to reproduce the annual cycle in southern polar cap column ozone. In the polar caps, the global mean column ozone is biased high. It does not prescribe solar cycle effects. The amplitude of the internally generated QBO signal in ozone is well represented, while the period is biased high. The tropical ENSO signal in temperature and ozone is within the cluster of model responses. The model uses optical properties from GISS and gives a close representation of observed ozone changes after volcanic eruptions. Overall, UMUKCA-METO simulates natural ozone variations well, with better or mean performance in most diagnostics.

UMUKCA-UCAM performs well to very well for the annual mean and annual cycle in ozone, in near global and northern polar column ozone. The variability of column ozone in the northern polar caps is well represented. The

model fails to reproduce the annual cycle in southern polar cap column ozone and variability. The global mean column ozone is biased high, everywhere. It only prescribes TSI changes and therefore misrepresents solar cycle effects. The amplitude of the QBO signal in ozone is well represented, while the period is biased high. The tropical ENSO signal in temperature and ozone is within the cluster of model responses. It does not include radiative effects of volcanic aerosols and it does not show a volcanic response. Overall, UMUKCA-UCAM simulates natural ozone variations with mixed and/or limited success.

WACCM accurately represents the annual mean and the annual cycle in ozone and in near global column ozone. The annual cycle in northern polar cap is well represented. The model fails to reproduce the annual cycle in the southern polar cap column ozone and in the variability of column ozone in both polar caps. It uses spectrally resolved solar irradiance data and is the model that best represents the solar cycle signal among the models considered here. The amplitude of the ozone response to the nudged QBO is moderately overestimated. The tropical ENSO signal in temperature and ozone is within the cluster of model responses. To represent volcanoes it uses optical properties derived from SPARC SADs and largely overestimates the temperature response after the Agung and Pinatubo eruptions. Overall, WACCM simulates natural ozone variations with mixed or in some diagnostics limited success.

References

- Angell, J. K., 1997. Estimated impact of Agung, El Chichón and Pinatubo volcanic eruptions on global and regional total ozone after adjustment for the QBO, *Geophys. Res. Lett.*, **24**, 647-650.
- Austin, J., L. L. Hood, and B. E. Soukharev, 2007. Solar cycle variations of stratospheric ozone and temperature in simulations of a coupled chemistry-climate model, *Atmos. Chem. Phys.*, **7**, 1693-1706.
- Austin, J., K. Tourpali, E. Rozanov, H. Akiyoshi, S. Bekki, G. Bodeker, C. Brühl, N. Butchart, M. Chipperfield, M. Deushi, V.I. Fomichev, M.A. Giorgetta, L. Gray, K. Kodera, D. Kinnison, E. Manzini, D. Marsh, K. Matthes, T. Nagashima, K. Shibata, R.S. Stolarski, H. Struthers, and W. Tian, 2008. Coupled chemistry climate model simulations of the solar cycle in ozone and temperature, *J. Geophys. Res.*, **113**, doi:10.1029/2007JD009391.
- Baldwin, M. P., L. J. Gray, T. J. Dunkerton, K. Hamilton, P. H. Haynes, W. J. Randel, J. R. Holton, M. J. Alexander, I. Hirota, T. Horinouchi, D. B. A. Jones, J. S. Kinnersley, C. Marquardt, K. Sato, and M. Takahashi, 2001. The Quasi-Biennial Oscillation, *Rev. Geophys.*, **39**, 179-229.
- Bodeker, G. E., J. C. Scott, K. Kreher, and R. L. McKenzie, 2001. Global ozone trends in potential vorticity coordinates using TOMS and GOME intercompared against the Dobson network: 1978-1998, *J. Geophys. Res.*, **106**, 23,029-23,042.
- Baldwin, M. P. and D. W. J. Thompson, 2009. A critical comparison of stratosphere-troposphere coupling indices, *Quart. J. Roy. Meteorol. Soc.*, **135**, 1661-1672.
- Bodeker, G. E., I. S. Boyd and W. A. Matthews, 1998. Trends and variability in vertical ozone and temperature profiles measured by ozonesondes at Lauder, New Zealand 1986-1996, *J. Geophys. Res.*, **103**, 28,661-28,681.
- Bodeker, G. E., Shiona, H., and Eskes, H., 2005. Indicators of Antarctic ozone depletion, *Atmos. Chem. Phys.*, **5**, 2603-2615.
- Brönnimann, S., J. Luterbacher, J. Staehelin, T. M. Svendby, G. Hansen, and T. Svenoe, 2004. Extreme climate of the global troposphere and stratosphere in 1940 - 42 related to El Nino, *Nature*, **431**, 971 - 974.
- Brönnimann, S., M. Schraner, B. Müller, A. Fischer, D. Brunner, E. Rozanov and T. Egorova, 2006. The 1986-1989 ENSO cycle in a chemical climate model, *Atmos. Chem. Phys.*, **6**, 4669-4685.
- Cagnazzo, C., E. Manzini, N. Calvo, A. Douglass, H. Akiyoshi, S. Bekki, M. Chipperfield, M. Dameris, M. Deushi, A. Fischer, H. Garny, A. Gettelman, M. A. Giorgetta, D. Plummer, E. Rozanov, T. G. Shepherd, K. Shibata, A. Stenke, H. Struthers, and W. Tian, 2009. Northern winter stratospheric temperature and ozone responses to ENSO inferred from an ensemble of Chemistry Climate Models. *Atmos. Chem. Phys. Discuss.*, **9**, 12141-12170,
- Calvo, N., M. A. Giorgetta, R. Garcia-Herrera, and E. Manzini, 2009. Nonlinearity of the combined warm ENSO and QBO effects on the Northern Hemisphere polar vortex in MAECHAM5 simulations, *J. Geophys. Res.*, **114**, doi:10.1029/2008JD011445.
- Camp, C. D., and K.-K. Tung, 2007. Stratospheric polar warming by ENSO in winter: A statistical study, *Geophys. Res. Lett.*, **34**, doi:10.1029/2006GL028521.
- Crooks, S. A., and L. J. Gray, 2005. Characterization of the

- 11-year solar signal using a multiple regression analysis of the ERA-40 data set, *J. Clim.*, **18**, 996-1015.
- Dameris, M., S. Matthes, R. Deckert, V. Grewe, and M. Ponater, 2006. Solar cycle effect delays onset of ozone recovery, *Geophys. Res. Lett.*, **33**, doi:10.1029/2005GL024741.
- Eyring, V., N. Butchart, D. W. Waugh, H. Akiyoshi, J. Austin, S. Bekki, G. E. Bodeker, B. A. Boville, C. Brühl, M. P. Chipperfield, E. Cordero, M. Dameris, M. Deushi, V. E. Fioletov, S. M. Frith, R. R. Garcia, A. Gettelman, M. A. Giorgetta, V. Grewe, L. Jourdain, D. E. Kinnison, E. Mancini, E. Manzini, M. Marchand, D. R. Marsh, T. Nagashima, P. A. Newman, J. E. Nielsen, S. Pawson, G. Pitari, D. A. Plummer, E. Rozanov, M. Schraner, T. G. Shepherd, K. Shibata, R. S. Stolarski, H. Struthers, W. Tian, and M. Yoshiki, 2006. Assessment of temperature, trace species, and ozone in chemistry-climate model simulations of the recent past, *J. Geophys. Res.*, **111**, doi:10.1029/2006JD007327.
- Eyring, V., D. W. Waugh, G. E. Bodeker, E. Cordero, H. Akiyoshi, J. Austin, S. R. Beagley, B. A. Boville, P. Braesicke, C. Brühl, N. Butchart, M. P. Chipperfield, M. Dameris, R. Deckert, M. Deushi, S. M. Frith, R. R. Garcia, A. Gettelman, M. A. Giorgetta, D. E. Kinnison, E. Mancini, E. Manzini, D. R. Marsh, S. Matthes, T. Nagashima, P. A. Newman, J. E. Nielsen, S. Pawson, G. Pitari, D. A. Plummer, E. Rozanov, M. Schraner, J. F. Scinocca, K. Semeniuk, T. G. Shepherd, K. Shibata, B. Steil, R. S. Stolarski, W. Tian, and M. Yoshiki, 2007. Multi-model projections of ozone recovery in the 21st century, *J. Geophys. Res.*, **112**, doi:10.1029/2006JD008332.
- Fioletov, V. E., G. E. Bodeker, A. J. Miller, R. D. McPeters and R. Stolarski, 2002. Global and zonal total ozone variations estimated from ground-based and satellite measurements: 1964-2000, *J. Geophys. Res.*, **107**, doi:10.1029/2001JD001350.
- Fischer, A. M., D. T. Shindell, B. Winter, M. S. Bourqui, G. Faluvegi, E. Rozanov, M. Schraner, and S. Brönnimann, 2008. Stratospheric winter climate response to ENSO in three chemistry-climate models, *Geophys. Res. Lett.*, **35**, doi:10.1029/2008GL034289.
- Fortuin, J. P. F., and H. Kelder, 1996. Possible links between ozone and temperature profiles, *Geophys. Res. Lett.*, **23**, 1517-1520.
- Fortuin, J. P. F., and H. Kelder, 1998. An ozone climatology based on ozonesonde and satellite measurements, *J. Geophys. Res.*, **103**, 31709-31734.
- Frame, T. H. A., and L.J. Gray, 2010. The 11-year solar cycle in ERA-40 data: an update to 2008, *J. Climate*, in press.
- Free, M. and D. Seidel, 2009. The observed ENSO temperature signal in the stratosphere. (accepted *J. Geophys. Res.*)
- Froidevaux, L., Y. B. Jiang, A. Lambert, N. J. Livesey, W. G. Read, J. W. Waters, R. A. Fuller, T. P. Marcy, P. J. Popp, R. S. Gao, D. W. Fahey, K. W. Jucks, R. A. Stachnik, G. C. Toon, L. E. Christensen, C. R. Webster, P. F. Bernath, C. D. Boone, K. A. Walker, H. C. Pumphrey, R. S. Harwood, G. L. Manney, M. J. Schwartz, W. H. Daffer, B. J. Drouin, R. E. Coffield, D. T. Cuddy, R. F. Jarnot, B. W. Knosp, V. S. Perun, W. V. Snyder, P. C. Stek, R. P. Thurstans, P. A. Wagner, 2008. Validation of Aura Microwave Limb Sounder stratospheric ozone measurements, *J. Geophys. Res.*, **113**, doi:10.1029/2007JD008771.
- Fusco, A. C., and Salby, M. L., 1999. Interannual variations of total ozone and their relationship to variations of planetary wave activity, *J. Clim.*, **12**, 1619 – 1629.
- Garcia-Herrera, R., N. Calvo, R. R. Garcia, and M. A. Giorgetta, 2006. Propagation of ENSO temperature signals into the middle atmosphere: A comparison of two general circulation models and ERA-40 reanalysis data, *J. Geophys. Res.*, **111**, doi:10.1029/2005JD006061.
- Garfinkel, C. I., and D. L. Hartmann, 2007. Effects of El Niño-Southern Oscillation and the Quasi-Biennial Oscillation on polar temperatures in the stratosphere, *J. Geophys. Res.*, **112**, doi:10.1029/2007JD008481.
- Giorgetta, M. A., E. Manzini, and E. Roeckner, 2002. Forcing of the quasi-biennial oscillation from a broad spectrum of atmospheric waves, *Geophys. Res. Lett.*, **29**, doi:10.1029/2002GL14756.
- Giorgetta, M. A., E. Manzini, E. Roeckner, M. Esch, and L. Bengtsson, 2006. Climatology and Forcing of the Quasi-Biennial Oscillation in the MAECHAM5 Model, *J. Clim.*, **19**, doi:10.1175/JCLI3830.1.
- Grant, W. B., E. V. Browell, J. Fishman, V. G. Brackett, R. E. Veiga, D. Nganga, A. Minga, B. Cros, C. F. Butler, M. A. Fenn, C. S. Long, and L. L. Stowe, 1994. Aerosol-associated changes in tropical stratospheric

- ozone following the eruption of Mount Pinatubo, *J. Geophys. Res.*, **99**, 8197-8211.
- Gray, L. J., J. Beer, M. Geller, J. D. Haigh, M. Lockwood, K. Matthes, U. Cubasch, D. Fleitmann, G. Harrison, L. Hood, J. Luterbacher, G. A. Meehl, D. Shindell, B. van Geel, and W. White, 2010. *Solar Influences on Climate, Reviews of Geophysics*, in press.
- Gray, L. J. and M. P. Chipperfield, 1990. On the interannual variability of trace gases in the middle atmosphere, *Geophys. Res. Lett.*, **17**, 933-936.
- Gray, L. J., S. J. Phipps, T. J. Dunkerton, M. P. Baldwin, E. F. Drysdale, and M. R. Allen, 2001. A data study of the influence of the equatorial upper stratosphere on northern hemisphere stratospheric sudden warmings, *Quart. J. Roy. Meteorol. Soc.*, **127**, 1985-2003.
- Gray, L. J., S. A. Crooks, M. A. Palmer, C. L. Pascow, and S. Sparrow, 2006. A possible transfer mechanism for the 11-year solar cycle to the lower stratosphere, *Space Sci. Rev.*, **125**, 357-370.
- Groß, J.-U., and J. M. Russell III, 2005. Technical note: A stratospheric climatology for O₃, H₂O, CH₄, NO_x, HCl and HF derived from HALOE measurements, *Atmos. Chem. Phys.*, **5**, 2797-2807.
- Haigh, J. D., M. Blackburn, and R. Day, 2005. The Response of Tropospheric Circulation to Perturbations in Lower-Stratospheric Temperature, *J. Clim.*, **18**, 3672-3685.
- Haigh, J. D., 1999. Modelling the impact of solar variability on climate. *J. Atmos. Sol. Terr. Phys.*, **61**, 63-72.
- Haimberger, L., C. Tavalato, S. Sperka, 2008. Towards elimination of the warm bias in historic radiosonde temperature records — some new results from a comprehensive intercomparison of upper air data. *J. Clim.*, **21**, 4587-4606.
- Hassler, B., G.E. Bodeker, I. Cionni, and M. Dameris, 2009. A vertically resolved, monthly mean ozone database from 1979 to 2100 for constraining global climate model simulations, *International Journal of Remote Sensing*, **30**, 4009-4018.
- Hoerling, M. P., Kumar, A. and Zhong, M., 1997. El Niño, La Niña, and the nonlinearity of their teleconnections. *J. Clim.*, **10**, 1769-1786.
- Hofmann, D. J., S. J. Oltmans, J. M. Harris, W. D. Komhyr, J. A. Lathrop, T. DeFoor, and D. Kuniyuki, 1993. Ozone measurements at Hilo, Hawaii following the eruption of Pinatubo, *Geophys. Res. Lett.*, **20**, 1555-1558.
- Hu, Y. and K.-K. Tung, 2002. Interannual and Decadal Variations of Planetary Wave Activity, Stratospheric Cooling, and Northern Hemisphere Annular Mode. *J. Clim.*, **15**, 1659-1673.
- Ito, K., Y. Naito, and S. Yoden, 2009. Combined effects of QBO and 11-year solar cycle on the winter hemisphere in a stratosphere-troposphere coupled system, *Geophys. Res. Lett.*, **36**, doi:10.1029/2008GL037117.
- Kalnay, E., M. Kanamitsu, R. Kistler, W. Collins, D. Deaven, L. Gandin, M. Iredell, S. Saha, G. White, J. Woolen, Y. Zhu, A. Leetmaa, R. Reynolds, M. Chelliah, W. Ebisuzaki, W. Higgins, J. Janowiak, K. C. Mo, C. Ropelewski, J. Wang, R. Jenne, and D. Joseph, 1996. The NCEP/NCAR 40-Year Reanalysis Project. *Bull. Amer. Meteor. Soc.*, **77**, 437-471.
- Kodera, K., and Y. Kuroda, 2002. Dynamical response to the solar cycle, *J. Geophys. Res.*, **107**, doi:10.1029/2002JD002224.
- Kodera, K., 2006. The Role of Dynamics in Solar Forcing, *Space Sci. Rev.*, **125**, 319-330.
- Kodera, K., K. Coughlin, and O. Arakawa, 2007. Possible modulation of the connection between the Pacific and Indian ocean variability by the solar cycle, *Geophys. Res. Lett.*, **34**, doi:10.1029/2006GL027827.
- Kryjov, V. N. and C.-K. Park, 2007. Solar Modulation of the El Niño/Southern Oscillation impact on the Northern Hemisphere Annular Mode. *Geophys. Res. Lett.*, **34**, doi: 10.1029/2006GL028015.
- Kuroda, K., 2007. Effect of QBO and ENSO on the Solar Cycle modulation of winter North Atlantic Oscillation. *J. Met. Soc. Japan*, **85**, 889-898.
- Labitzke, K., 1987. Sunspots, the QBO and the stratospheric temperature in the north polar region, *Geophys. Res. Lett.*, **14**, 535-537.
- Labitzke, K., and H. van Loon, 1988. Associations between the 11-year solar cycle, the QBO and the atmosphere, Part I: The troposphere and stratosphere in the northern hemisphere in winter, *J. Atmos. Terr. Phys.*, **50**, 197-206.
- Lee, H. and A. K. Smith, 2003. Simulation of the combined effects of solar cycle, quasi-biennial oscillation, and volcanic forcing on stratospheric ozone changes in recent decades, *J. Geophys. Res.*, **108**, doi:10.1029/2001JD001503.
- Manzini, E., 2009. ENSO and the stratosphere. *Nature*

- Geosci.*, **2**, 749-750.
- Manzini, E. M. A. Giorgetta, M. Esch, L. Kornblueh, and E. Roeckner, 2006. The influence of sea surface temperatures on the Northern winter stratosphere: Ensemble simulations with the MAECHAM5 model, *J. Clim.*, **19**, 3863-3881.
- Marsh, D. R., and R. R. Garcia, 2007. Attribution of decadal variability in lower-stratospheric tropical ozone, *Geophys. Res. Lett.*, **34**, doi:10.1029/2007GL030935.
- Matthes, K., Y. Kuroda, K. Kodera, and U. Langematz, 2006. Transfer of the solar signal from the stratosphere to the troposphere: Northern winter, *J. Geophys. Res.*, **111**, doi:10.1029/2005JD006283.
- Matthes, K., K. Kodera, L.J. Gray, et al., 2007: Report on the first solar influence for SPARC (SOLARIS) workshop in Boulder/CO October 3-6 2006, SPARC Newsletter 28.
- Matthes, K., U. Langematz, L.J. Gray, K. Kodera, and K. Labitzke, 2004. Improved 11-Year Solar Signal in the Freie Universität Berlin Climate Middle Atmosphere Model (FUB-CMAM), *J. Geophys. Res.*, **109**, doi:10.1029/2003JD004012.
- Matthes, K., D. R. Marsh, R. R. Garcia, D. Kinnison, F. Sassi, and S. Walters, 2010. The role of the QBO in modeling the influence of the 11-year solar cycle on the atmosphere using constant forcings, revised for *J. Geophys. Res.*
- Matthes, K., K. Kodera, J.D. Haigh, D.T. Shindell, K. Shibata, U. Langematz, E. Rozanov, and Y. Kuroda, 2003. GRIPS solar experiments intercomparison project: Initial results, *Pap. Meteorol. Geophys.*, **54**, 71-90.
- Newman, P. A., J. S. Daniel, D. W. Waugh, and E. R. Nash, 2007. A new formulation of equivalent effective stratospheric chlorine (EESC), *Atmos. Chem. Phys.*, **7**, 4537-4552.
- Newman, P., E. Nash, and J. Rosenfield, 2001. What controls the temperature of the Arctic stratosphere during the spring?, *J. Geophys. Res.*, **106**, 19999-20010.
- Newman, P., and W. J. Randel, 1988. Coherent ozone dynamical changes during the Southern hemisphere spring, 1979-1988. *J. Geophys. Res.*, **93**, 12585-12606.
- Punge, H.J., and M. A. Giorgetta, 2008. Net effect of the QBO in a chemistry-climate model, *Atmos. Chem. Phys.*, **8**, 6505-6525.
- Randel, W. J., Wu, F., and Stolarski, R., 2002. Changes in column ozone correlated with the stratospheric EP flux, *J. Meteorol. Soc. Japan*, **80**, 849-862.
- Randel, W. J. and F. Wu, 2007. A stratospheric ozone profile data set for 1979-2005: variability, trends, and comparisons with column ozone data, *J. Geophys. Res.*, **112**, doi:10.1029/2006JD007339.
- Randel, W. J., K. P. Shine, J. Austin, J. Barnett, C. Claud, N. P. Gillett, P. Keckhut, U. Langematz, R. Lin, C. Long, C. Mears, A. Miller, J. Nash, D. J. Seidel, D. W. J. Thompson, F. Wu, and S. Yoden, 2009a. An update of observed stratospheric temperature trends, *J. Geophys. Res.*, **114**, doi:10.1029/2008JD010421.
- Randel, W. J., R. R. Garcia, N. Calvo, and D. Marsh, 2009b. ENSO influence on zonal mean temperature and ozone in the tropical lower stratosphere, *Geophys. Res. Lett.*, **36**, doi:10.1029/2009GL039343.
- Randel, W. J., F. Wu, J. M. Russell III, J. W. Waters, and L. Froidevaux, 1995. Ozone and temperature changes in the stratosphere following the eruption of Mount Pinatubo, *J. Geophys. Res.*, **100**, 16753-16764.
- Russell, J. M., III, L. L. Gordley, J. H. Park, S. R. Drayson, W. D. Hesketh, R. J. Cicerone, A. F. Tuck, J. E. Frederick, J. E. Harries, P. J. Crutzen, 1993. The Halogen Occultation Experiment, *J. Geophys. Res.*, **98**, 10,777-10,797.
- Sassi, F., D. Kinnison, B. A. Boville, R. R. Garcia, and R. Roble, 2004. Effect of El Niño-Southern Oscillation on the dynamical, thermal, and chemical structure of the middle atmosphere, *J. Geophys. Res.*, **109**, doi:10.1029/2003JD004434.
- Scaife, A., N. Butchart, C. Warner, D. Staniforth, W. Norton, and J. Austin, 2000. Realistic Quasi-Biennial Oscillation in a simulation of the global climate, *Geophys. Res. Lett.*, **27**, 3481-3484.
- Shibata, K., and M. Deushi, 2005. Partitioning between resolved wave forcing and unresolved gravity wave forcing to the quasi-biennial oscillation as revealed with a coupled chemistry-climate model, *Geophys. Res. Lett.*, **32**, doi:10.1029/2005GL022885.
- Solomon, S., R. W. Portmann, R. R. Garcia, W. Randel, F. Wu, R. Nagatani, J. Gleason, L. Thomason, L. R. Poole, and M. P. McCormick, 1998. Ozone depletion at mid-latitudes: coupling of volcanic aerosols and temperature variability to anthropogenic chlorine, *Geophys. Res. Lett.*, **25**, 1871-1874.

- Smith, A. K., and K. Matthes, 2008. Decadal-Scale Periodicities in the Stratosphere Associated with the 11-Year Solar Cycle and the QBO, *J. Geophys. Res.*, **113**, doi:10.1029/2007JD009051.
- Steinbrecht, W., Hassler, B., Brühl, C., Dameris, M., Giorgetta, M. A., Grewe, V., Manzini, E., Matthes, S., Schnadt, C., Steil, B., and Winkler, P., 2006. Interannual variation patterns of total ozone and temperature in observations and model simulations, *Atmos. Chem. Phys.*, **6**, 349–374.
- Stolarski, R. S. and S. Frith, 2006. Search for evidence of trend slow-down in the long-term TOMS/SBUV total ozone data record: the importance of instrument drift uncertainty and fingerprint detection, *Atmos. Chem. Phys.*, **6**, 3883-3912.
- Taylor, K. E., 2001. Summarizing multiple aspects of model performance in a single diagram, *J. Geophys. Res.*, **106**, 7183-7192.
- Thomason, L., and T. Peter, 2006. Assessment of Stratospheric Aerosol Properties (ASAP), SPARC Report No. 4., WCRP-124, WMO/TD-No. 1295.
- Tie, X. X., and G. P. Brasseur, 1995. The response of stratospheric ozone to volcanic eruptions: Sensitivity to atmospheric chlorine loading, *Geophys. Res. Lett.*, **22**, 3035-3038.
- Timmreck, C., H.-F. Graf and B. Steil, 2003. Aerosol chemistry interactions after the Mt. Pinatubo eruption, in *Volcanism and the Earth's Atmosphere*, eds. A. Robock and C. Oppenheimer, AGU Monograph, Vol. 139, p213-225.
- Uppala, S., et al., 2004. ERA-40: ECMWF 45-year reanalysis of the global atmosphere and surface conditions 1957–2002: ECMWF Newsletter, Vol. 101, ECMWF, Reading, United Kingdom, 2–21.
- Van Loon, H., and K. Labitzke, 1987. The southern oscillation. Part V: The anomalies in the lower stratosphere of the Northern Hemisphere in winter and a comparison with the quasi-biennial oscillation. *Mon. Wea. Rev.*, **115**, 357–369.
- Waters, J. W., Froidevaux, L., Harwood, R.S., Jarnot, R.F., Pickett, H.M., Read, W.G., Siegel, P.H., Cofield, R.E., Filipiak, M.J., Flower, D.A., Holden, J.R., Lau, G.K., Livesey, N.J., Manney, G.L., Pumphrey, H.C., Santee, M.L., Wu, D.L., Cuddy, D.T., Lay, R.R., Loo, M.S., Perun, V.S., Schwartz, M.J., Stek, P.C., Thurstans, R.P., Boyles, M.A., Chandra, K.M., Chavez, M.C., Gun-Shing Chen, Chudasama, B.V., Dodge, R., Fuller, R.A., Girard, M.A., Jiang, J.H., Yibo Jiang, Knosp, B.W., LaBelle, R.C., Lam, J.C., Lee, K.A., Miller, D., Oswald, J.E., Patel, N.C., Pukala, D.M., Quintero, O., Scaff, D.M., Van Snyder, W., Tope, M.C., Wagner, P.A., and Walch, M.J., 2006. The Earth Observing System Microwave Limb Sounder (EOS MLS) on the Aura Satellite, *IEEE Trans. Geosci. Remote Sens.*, **44**, 1075-1092.
- Weber, M., S. Dhomse, F. Wittrock, A. Richter, B.-M. Sinnhuber and J. P. Burrows, 2003. Dynamical control of NH and SH winter/spring total ozone from GOME observations in 1995-2002, *Geophys. Res. Lett.*, **30**, doi:10.1029/2002GL016799.
- World Meteorological Organization (WMO)/United Nations Environment Programme (UNEP), 2007. *Scientific Assessment of Ozone Depletion: 2006*, World Meteorological Organization, Global Ozone Research and Monitoring Project, Report No. 50, Geneva, Switzerland.